USING THE COUPLED MICRO-REACTOR/UHV SURFACE ANALYSIS SYSTEM AND THE QCM-BASED VISCOUS FLOW REACTOR TO STUDY AREA-SELECTIVE DEPOSITION

A Thesis

Presented to the Faculty of the Graduate School

of Cornell University

In Partial Fulfillment of the Requirements for the Degree of

Master of Science

by

Yen-Hsiung Wang

August 2021

ABSTRACT

Patterning during a nanofabrication process could be designed with a variety of techniques to manifest spatial control of chemical reactions and it is categorized as a top-down or a bottom-up process in general. While the state-of-the-art top-down techniques meet challenges, a bottom-up deposition process shows advantages in some aspects. In our research, we focus our work on modified process of atomic layer deposition (ALD) and chemical vapor deposition (CVD) to achieve area-selective deposition (ASD).

We have been trying to find a pathway to achieve ASD with the formation of a reversible blocking layer exclusively on the non-growth surface. During the deposition process, a third gas-phase molecule, what we refer to as “co-adsorbate”, is introduced to compete for adsorption sites on the non-growth surface while leave precursor adsorption unimpeded on the growth surface. It is a very promising approach mainly due to the self-aligning and high-throughput essence.

BIOGRAPHICAL SKETCH

Yen-Hsiung Wang was born and raised in Taoyuan, a city in the northern part of Taiwan. He had received education for 20 years in this city and had cultivated his passion and interest in the immense science world. With his parents nurturing, he is motivated to have a goal of studying abroad in the future. He then had the opportunities to attend National Taiwan University (NTU) for bachelor degree, majoring in chemical engineering. He had joined Prof. Nae-Lih Wu's group at NTU and conducted independent studies on several interesting Li-ion battery related projects in which he could embody the knowledge he has learned. Beyond academic work, he has shown his enthusiasm in dancing and participated in a few performances, which he had also choreographed some of them. For the next chapter of his life, he had started to portrait the career and was fascinated by the advanced technology of semiconductor foundries industry in Taiwan. With the financial support from his parents, he then pursued a Master degree of chemical engineering at Cornell University with the guidance from Prof. James R. Engstrom. He had the chance to conduct the research of a very innovated pathway to achieve area-selective thin film deposition and experience hands-on operation of various hardware. With great resources at Cornell, he has learned in-depth knowledge of nanoelectronics and semiconductor. He had joined an internship and is excited to join as process engineer at Taiwan Semiconductor Manufacturing Company at Phoenix, Arizona in October, 2021.

Dedicated to my family and all of my intimate friends

for all the unconditional love and support

ACKNOWLEDGMENTS

First and foremost, I want to thank my advisor, Prof. James R. Engstrom, who has provided countless and valuable teaching and guidance throughout my researching program. Not only has he shared his knowledge related to the ultra-high vacuum system, but has taught us the thinking process for fault analysis, which is the core value that an experimentalist should have. “Work smart. Be thorough. Work as a team. Strive for quality.”, he said as the group motto. I also want to thank Prof. Robert A. DiStasio Jr. for all the insightful inputs throughout his collaboration with us and the instruction on the simulation project I have participated in with the help from Yan Yang, the PhD student from DiStasio group.

Importantly, I want to express my deepest gratitude to my parents, An-Ming Wang and Hsiu-Min Li, who have made great efforts to support our family and have realized the journey of me studying abroad. It is their eternal love and absolute devotion that nurture my sister, Lu-Chiao Wang, and I; thus I could pursue scientific knowledge unfettered. I will always keep their inculcation in mind and continue on my life adventure with it. They are the love of my life.

Last but not least, I would like to acknowledge all alumni members from Engstrom Research Group (ERG). They have passed down the wisdom and all the incredible lab work that has been established. It is the very foundation of all of my research work. In particular, Taewon Suh has given me seamless assistance within and beyond academic work. He is extremely clever and strong on execution and he is the role model of mine. I also want to thank Colleen Lawlor, Pengyuan Zhao, Vidyesh Parampalli Madhyastha and Ziwen Xin for being such hospitable colleagues throughout my program. Their intelligence is absolutely I admire of. It is very fortunate to have worked with them.

TABLE OF CONTENTS

LIST OF FIGURES

LIST OF TABLES

LIST OF ABBREVIATIONS AND SYMBOLS

ALD	atomic layer deposition
Ar	Argon
ARXPS	angle-resolved X-ray photoelectron spectroscopy
BE	binding energy
chemox	chemical oxide
CFD	computational fluid dynamics
Co	cobalt
CR	cooling rate
Cu	copper
DFT	density functional theory
fcc	face centered cubic
GPC	growth per cycle
hcp	hexagonal close packed
LEISS	low-energy ion scattering spectrometer
m/z	mass-to-charge ratio
Mo	molybdenum
PSU	power supply unit
PVD	physical vapor deposition
QCM	quartz crystal microbalance
QMS	quadruple mass spectrometer
SA	simulated annealing
TDMAZ	tetrakis(dimethylamido)zirconium (IV)
TEMAHf	tetrakis(ethylmethylamido) hafnium (IV)

TEMAZ	tetrakis(ethylmethylamido) zirconium (IV)
UHV	ultra-high vacuum
UV	ultraviolet
XPS	X-ray photoelectron spectroscopy

1. Introduction

1.1 Background

The evolution of semiconductor has contributed to the advance of technology in every aspect throughout the human history. From the most rudimental concept of semiconductor documented as Faraday effect, the development of not only the basic devices but the theory has given rise to the more sophisticated fabrication and application of the microelectronics. The theory of p-n junction and the junction transistors were presented to the world by William Shockley, John Bardeen and Walter Brattain, who received the Nobel Prize in physics in 1956. The inception of integrated circuit has been established with the more efficient transistors and Jack Kilby has received the Nobel Prize in physics for this accomplishment in 2000. The development of transistor fabrication technologies and 3D structure designs has continued since then, including metal-oxide-semiconductor field-effect transistor (MOSFET), FinFET, gate-all-around (GAA) and more recent techniques involving quantum wire and quantum dots. Plus the knowledge of silicon-on-insulator (SOI) and more prospective 3D packaging techniques, Gordan Moore has proposed in 1965 that the total number of transistors which could be fabricated into the integrated circuit would increase exponentially [1].

Consequently, nanoscale and sub-nanoscale patterning are more critical in the fabrication process; in the meanwhile, such process is expected to accommodate high-throughput manufacturing to meet the growing demand. Photolithography, which is described as a “top-down” process, has met with the challenges, like misalignment, since the technique has altered in order to reach the high resolution for miniaturization. Although lithography with

deep UV (193 nm) and extreme UV (13.5 nm) has developed over the years, cost has increased due to multiple steps of exposure, engineering of photoresist, mask, etc. In contrast, area-selective deposition (ASD), a "bottom-up" process, has become dominant for chemical patterning due to less consumption of chemicals and energy [2,3]. To achieve area selectivity, chemical reactions between gas-phase species and surface reaction sites are utilized to demonstrate specificity. That is, in contrast to isotropic deposition by sputtering and physical vapor deposition (PVD), atomic layer deposition (ALD) and chemical vapor deposition (CVD) are focused in this study. Specifically, among various ASD techniques, the modified gas-phase CVD and ALD processes discussed herein are explored by the competitive adsorption of the third species, a co-adsorbate, in order to deposit directly on the growth surface and impede film growth on other substrate species. More details will be discussed in the following sections.

1.2 Chemical vapor deposition (CVD) and atomic layer deposition (ALD)

Microscopically, film deposition involves gas-phase species nucleation on the surface initially [2]. The heated reactive molecules will first be brought to the surface by a flux of carrier gas after either decomposition or not. The kinetics and the flow dynamics of the reactants play a vital part in the real-world reaction since it determines the partial pressure (concentration), impinging rate and directionality at the surface for reaction. Impinging on the surface, the molecules would subject to various interaction mechanism with the reaction sites on the surface illustrated in Fig. 1-1 [2]. Physisorption is relatively weaker than chemisorption since the former stems from the dipoles among the molecules and the latter occurs when electrons are shared (re-hybridization). Thus, after a physisorption, chances are the molecules diffuse on the surface to search for favorable sites and further nucleate with the same species or react with another

species. This concept of thermodynamic driving forces is rather important not solely for deposition, but for area-selective mechanism since the initial nucleation could be inhibited by different approaches.

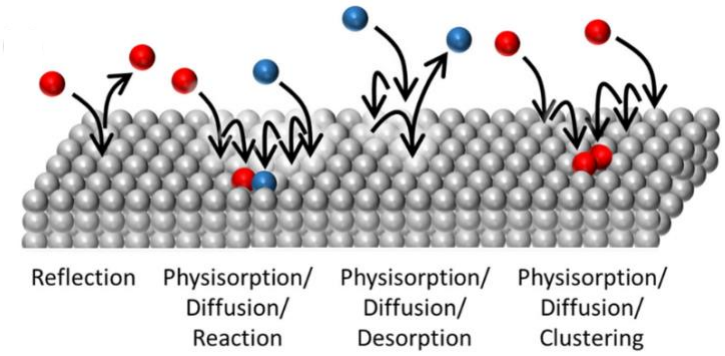

Figure 1-1 Schematic of possible interactions and mechanisms for nuclei formation among the adsorbate and surface atoms

CVD process describes a more general reaction mechanism while multiple reactants are introduced into the reaction zone. In a typical CVD process with precursor and co-reactant, the kinetics of the two reactant fluxes dominates the film growth since the nucleation process is expedited by the reaction between the two species at the surface. A plasma-enhanced CVD is employed with a plasma species (either precursor or co-reactant) that could not only increase the partial pressure of reactive species but, at the same time, accelerate the reaction rate by physical bombardment and the reactive free radicals. Due to its higher deposition rate and thus higher throughput, it is broadly applied in the industry for dielectric compounds, such as organosilicate (SiOCH) glass as low-k material. On the other hand, a CVD process is likely to be susceptible to amorphous growth and incorporating impurities since the desorption of by-

products might be not effective, especially under atmospheric pressure (APCVD). The scope of our study is in the range of low pressure (LPCVD) and includes the modified CVD process for ASD with the introduction of the third species, which will be discussed in later sections.

Unlike CVD, cycles of exposure and purge as sequential steps are demonstrated in an ALD process. A typical ALD involves precursor exposure, purge, co-reactant exposure and then purge. Purging with inert gas is relatively indispensable in order to clean the surface (eliminate the weakly bonded by-products or residuals) with convection and ideally leaves only a single kind of surface species at any time. As a result, the precursor should be intrinsically self-limiting; that is, the precursor will not react with the chemisorbed itself. An example of proposed ALD mechanism with tetrakis(dimethylamido)zirconium (TDMAZ) and water is illustrated in Fig. 1-2 [4]. A monolayer will form once the coverage of the surface sites are saturated, while molecules have gone through multiple steps of adsorption/desorption and diffusion in search for energetically favorable sites. ALD is thus known for excellent thickness controlling and producing a conformal thin film deposition especially on 3D structures with a high aspect ratio; on the other hand, low throughput is the disadvantage. The chemistry of ALD could be simpler than that of CVD due to less gas-phase interaction and the species homogeneity at the surface, which renders an ideal foundation for ASD study. The substrate temperature cannot be stressed enough since various physical change or chemical reaction and GPC could be observed as shown in Fig. 1-3. It is an important parameter in this ASD study within the ALD window with the co-adsorbate, which will be discussed in Ch. 1.4.

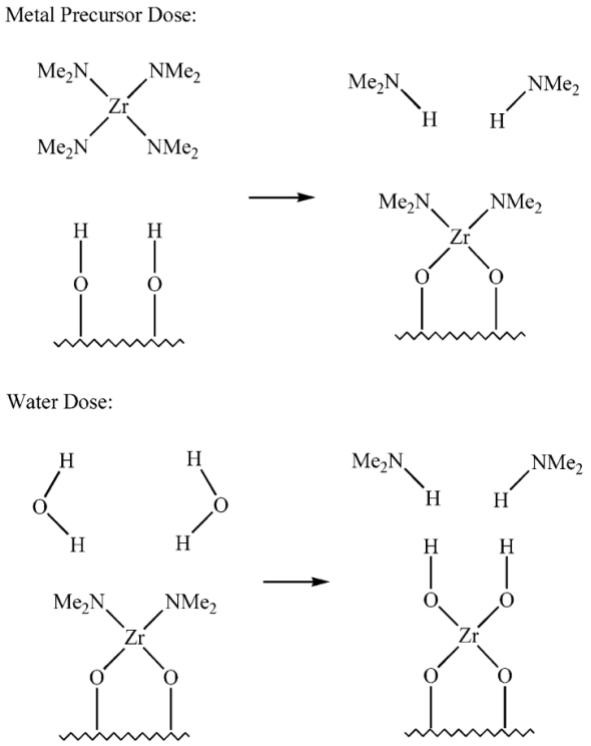

Figure 1-2 Schematic of the proposed ideal ALD mechanism with TDMAZ and water at respective steps

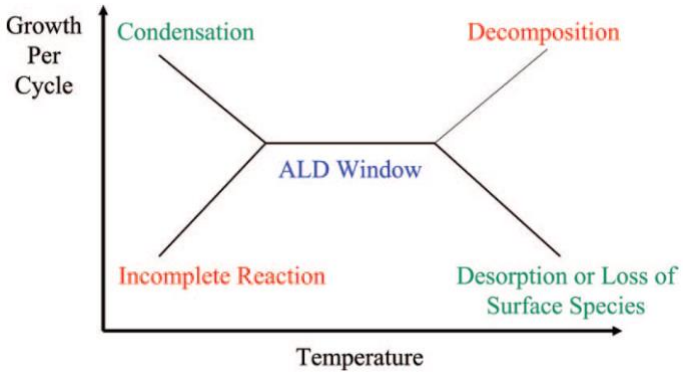

Figure 1-3 Schematic of ALD window and possible ALD behavior under different substrate temperature

1.3 Area selective deposition (ASD)

As mentioned before, ASD is mostly observed with the inherent selectivity among the species or selective functionalization on the starting surface. The nucleation delay could then further lead to the differential of film growth among different substrates. According to the deposited film and substrate types for numerous applications, ASD is generally categorized as DoD, MoM, DoM, MoD, SoS, MoS, DoS (D: dielectric / M: metal / S: semiconductor / o: on), etc. The quantification for selectivity (S) is generally defined as

$$S = \frac{\theta_{GA} - \theta_{NGA}}{\theta_{GA} + \theta_{NGA}} \approx \frac{t_{GA} - t_{NGA}}{t_{GA} + t_{NGA}} \quad (1)$$

where θ_{GA} and θ_{NGA} represents the net surface coverage on the growth and non-growth area respectively. Thicknesses on the respective surfaces (t_{GA} and t_{NGA}) are also used in some work for simplification [2,5]. The selectivity is systematically concluded to be the function of ALD cycle number or the length of CVD process.

Various approaches have been studied to achieve ASD. Inherent selective deposition directly utilizes the intrinsic chemical reactivities, which could be classified as a selective precursor adsorption or a selective co-reactant adsorption. Typical examples for the former have been demonstrated with metal oxide (such as TiO_2, Al_2O_3, HfO_2, and so on) deposited selectively between hydroxyl group (OH-Si) and hydrogen (H-Si) terminated silica surface [6,7]. As for the latter, the studies utilizes the catalytic nature of the noble metal to some gases so that

the dissociated monoatomic species that has selectively adsorbed on the surface is served as the co-reactant for deposition, such as O_2 on Pt [8].

Another well-studied approach is the selective functionalization on the surface prior to deposition by using self-assembly monolayers (SAM) [9–11], polymer [12,13], thin organic films [14], etc. Typically, the modification is to alter the surface to one that is terminated with less reactive groups. Take ASD with SAM or polymer for instance, the monomer comprises of a head group that could chemisorb on the origin surface and a tail group (new surface group) defined to be inert to deposition process, such as $-CH_3$ or $-CF_3$ [9]. Besides depositing an additional film, some techniques, which are known as topographically selectivity, involve surface pre-treatments to modify the surface group and thus alter the reactivity. Process like H_2 plasma is used to reduce the amorphous carbon surface and thus make the surface terminated with $-CH_3$ [15]. There are also several downsides for these methods, such as the low throughput in manufacturing if aqueous or spin-on process with solvent is involved. Post-treatments for reversing the surface (i.e., post deposition processes like elimination of the residuals and surface recovery after plasma treatment) should also be considered since the semi-finished products have to be tolerable for the numerous fabrication steps afterward and maintained at high purity.

As a result, a different path way for ASD by the so-called competitive adsorption is the objective of this study. Unlike the techniques mentioned before, this study investigates whether the co-exposure of the precursor and co-adsorbate (the third gas-phase species) could lead to the formation of a reversible blocking layer on the non-growth surface by the latter. The reversibility of the blocking layer is expected to be accomplished by just purging with inert gas; thus, the interaction should be chemisorption which is not so energetically favorable

(physisorption will be too weak). In the meanwhile, the adsorption energy of it on the non-growth surface should be distinctly stronger than the others so that the formation of blocking layer is exclusive. Additionally, since the gas-phase reactants are expected to be homogeneously mixed, there should be no chemical reaction among it and the reactants. Lastly, the surface termination should be inert to the deposition; i.e., it should be able to form a potent blocking layer without any deposition on top. As a result, the conditions impose highly specific requirements on the co-adsorbate, which involves at least 5 interactions illustrated in Fig. 1-4 when considering just two kinds of substrate species. On the other hand, the greatest potential of this approach is that it is a whole gas-phase process and thus the high throughput makes it much more viable to be applied in a manufacturing process. The blocking mechanism is not expected to alter the surface destructively or thoroughly as well.

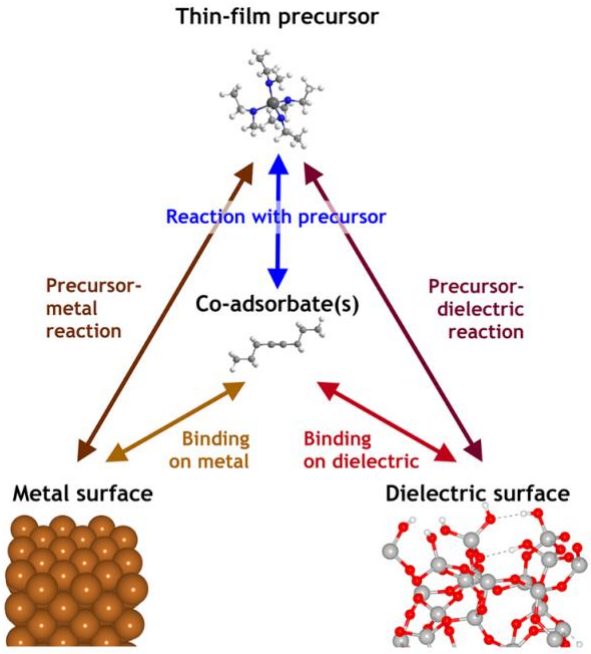

Figure 1-4 Schematic of the interactions when conducting a competitive adsorption to achieve ASD by introducing co-adsorbate

1.4 Langmuir isotherm

The adsorption mechanism of co-adsorbate on the non-growth surface could be depicted by the Langmuir isotherm model (Eq. 2). Under the ideal case, the co-adsorbate molecules behave as ideal gas and adsorb solely on the finite and homogeneous surface sites reversibly. The Gibbs free energy of co-adsorbate adsorption is assumed to be much lower than that of precursor. On top of this, after the adsorption, the co-adsorbate is expected not to diffuse or dissociate. Thus, a monolayer of adsorbed co-adsorbate, the blocking layer, will form once the sites are fully occupied. In reality, the lingering bulky functional groups from co-adsorbate could be served as protective group and hinder any further adsorption as well. The theoretical analysis including Van't Hoff equation (Eq. 3) is shown in Eq. 4.

$$K_{eq} = \frac{\theta}{p_A (1-\theta)} \tag{2}$$

$$\ln(K_{eq}) = -\frac{\Delta H_{ads}}{RT_s} + \frac{\Delta S_{ads}}{R} \tag{3}$$

$$\ln(p_A) = \frac{\Delta H_{ads}}{RT_s} + \ln\left[\frac{\theta}{(1-\theta)}\right] - \frac{\Delta S_{ads}}{R} \tag{4}$$

where

K_{eq}	: the equilibrium constant of adsorption	(Pa^{-1})
p_A	: the pressure of co-adsorbate	(Pa)
R	: gas constant	($J\text{-}K^{-1}\text{-}mol^{-1}$)
T_s	: the surface temperature of the substrate	(K)
ΔH_{ads}	: the enthalpy of adsorption	($J\text{-}mol^{-1}$)
ΔS_{ads}	: the entropy of adsorption	($J\text{-}K^{-1}\text{-}mol^{-1}$)

θ : the fraction of occupied surface sites (-)

Consequently, with the critical surface coverage θ_c (typically 0.999) and the values of adsorption enthalpy and entropy on respective substrate species (from DFT calculation in our study), the area selective window could be defined on the plot of $\log(p_A)$ versus $1/T_s$. An example of θ_c at 0.999 on copper and silica surfaces is shown in Fig. 1-5. Moreover, the scope of the model could be expanded with multiple surfaces to explore different process phases. However, this model has oversimplified the process. For example, the interactions (e.g. Lennard-Jones potential) among the adsorbed species might repel the adsorbates and thus reduce the coverage. Catalytic reaction between chemisorbed co-adsorbate and metal substrate might lead to low coverage and unwanted by-products, like acetylene (unsaturated hydrocarbon) on cobalt [16]. Nonetheless, the model could guide us through experimental works with the two key parameters, the partial pressure of co-adsorbate and substrate temperature.

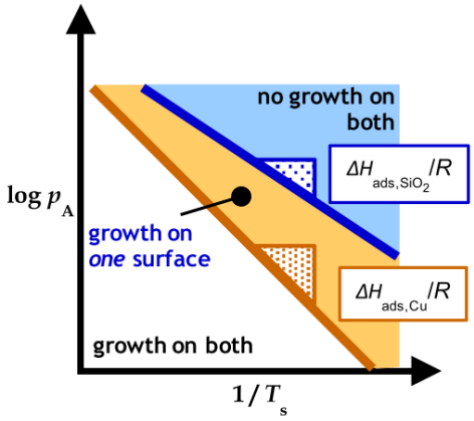

Figure 1-5 Schematic of area-selective window (orange shaded region) based on Langmiur model

1.5 ALD in high-κ film deposition

For the contemporary design for field effect transistors, such as complementary metal-oxide-semiconductor (CMOS) integrated circuits and MOSFETs, the choice of gate oxide has moved on to high-κ oxides, which have the property of higher permittivity than the typical silica. As the devices miniaturized, the thickness of the gate oxide is suppressed; however, the threshold of the leakage current due to electrons tunneling from the metal contact into the channel is much lower. This effect undermines performance and the ON-OFF ratio of drain current. The equivalent thickness of silica that could result in high leakage current is approximately 1.2 nm [17]. To maintain or improve the drain current at ON state, the capacitance density of the gate oxide is required to be large enough. While there is a limitation of the thickness, the alternative way is to choose a high-κ material. HfO_2 and ZrO_2 have emerged to become the potent candidates to replace silica. Both of them have sufficiently high dielectric constant (~ 22-25) and wide bandgaps (~ 5.0-7.0 eV) that could augment the threshold to leakage current [17,18].

From the perspective of fabrication, the module has transitioned from diffusion to film deposition techniques to deposit metal oxides instead of silica on doped silicon. The modern 3D structure, such as FinFET and GAA, demands that the gate oxide be deposited conformally and uniformly on the high aspect ratio substrate. On top of that, the precise control of thickness makes ALD the most implemented approach when it comes to gate oxide deposition [19,20]. On the other hand, there are still some practical problems, like the incorporation of the impurities. This issue is mostly associated with the ligands of the precursor and it would eventually result in the increase of dielectric constant and thus be detrimental to the performance of the transistor

[3,20]. Studies for novel and effective precursors, like tetrakis(tetrahydroborato)hafnium [$Hf(BH_4)_4$], have also been the important topic either in the industry or academia [4,18,21]. Although not a direct application of deposition, a study has shown that using TMA and water to employ Al_2O_3 ALD on high-κ/Ge devices on which the deposited alumina is served as the reductant to the oxidized surface of the substrate and a surface passivation layer [22]. Similarly, a knowledge has been imparted to us through the courtesy of Prof. Gregory N. Parsons that the exposure of TMA to the reactor could passivate the adsorbed water vapor and certain oxides deposited on the wall. This procedure has proved to be effective to suppress the lingering species in the system, especially for a hot-wall system, and retain the reproducibility of the reactor.

1.6 Density functional theory (DFT) calculation

The entropy and enthalpy of potential co-adsorbate adsorbing on silica, cobalt and copper surfaces are supported by the dispersion-inclusive DFT calculation from DiStasio Research Group from the Department of Chemistry at Cornell University [23]. The feasibility of selective deposition could be extracted from the calculated results, including the adsorption enthalpy, the bond length of the 4-octyne triple bond and the bond angle between the two unsaturated carbons and the adjacent saturated carbon. The results with T_s at 120°C and p_A at 0.36 Torr on hydroxyl-terminated amorphous silica, copper and cobalt are summarized in Table. 1-1 [23] and 1-2. The mean values of binding energy on respective substrates are -13.58 kcal-mol^{-1}, -39.66 kcal-mol^{-1} and -60.20 kcal-mol^{-1} (the work focuses on hcp Co since the phase transition to fcc occurs around 700K, which is outside of our scope [24]). Based on the substantial difference, the adsorption on silica is more like a typical physisorption while chemisorption could be foreseen on the metal surfaces. As references, the typical bond length and angle of C≡C in acetylene are

1.21Å and 180° while those of C=C in ethylene is 1.34Å and 121.3°, and 1.40Å and 120.0° in benzene. Those of C≡C in 4-octyne are 1.21Å and 178.8°. Consequently, after physisorption on silica, 4-octyne is predicted to remain its structure without rehybridization. On the other hand, the chemisorption on both the metal surfaces is supported by the longer triple bonds and the angles indicate that the triple bond (sp) could rehybridize with metal atom into double bond (sp^2). In the meanwhile, the sp^2 product is not robustly stable at the time scale of deposition experiment and thus the reaction could be demonstrated as reversible, which is a promising pathway to perform selective deposition and the surface could be recovered theoretically by purging. The adsorption energy on cobalt is calculated to be stronger than that on copper, which suggests that there might be catalytic reactions instead. Future experiments are required to explore the possibility on cobalt.

System	ΔU^{DFT} (kcal-mol^{-1})	ΔH (kcal-mol^{-1})	ΔG (kcal-mol^{-1})	C≡C (Å)	C−C≡C (°)
4-octyne	-	-	-	1.21	178.8
SiO_2 (Binding Motif #1)	-12.06	-11.28	15.79	1.22	177.6
SiO_2 (Binding Motif #2)	-13.71	-12.25	10.89	1.22	175.4
SiO_2 (Binding Motif #3)	-14.96	-15.13	16.76	1.20	174.4
Mean (SiO_2)	**-13.58 ± 1.45**	**-12.89 ± 2.00**	**14.48 ± 3.15**	**1.21 ± 0.01**	**175.8 ± 1.6**
Cu(111) Long Bridge	-39.70	-39.84	-5.92	1.37	126.5
Cu(110) Long Bridge	-35.68	-37.21	-2.88	1.38	123.0
Cu(100) Long Bridge	-42.06	-42.85	-12.46	1.37	125.8
Cu(100) Short Bridge	-41.19	-42.02	-11.23	1.38	124.1
Mean (Cu)	**-39.66 ± 2.83**	**-40.48 ± 2.52**	**-8.12 ± 4.50**	**1.38 ± 0.01**	**124.9 ± 1.6**

Table 1-1 Electronic binding energies (ΔU^{DFT}), binding enthalpies [$\Delta H(T,p_A)$], and binding Gibbs free energies [$\Delta G(T,p_A)$] for the selected binding motifs of 4-octyne on an amorphous hydroxyl-terminated SiO_2 surface and the high- symmetry/low-index facets of Cu

Surface	ΔU (kcal/mol)	C≡C (Å)	C-C≡C (°)
Co(111)	-64.90	1.39	127.90
Co(0001)	-60.20	1.41	121.96

Table 1-2 Electronic binding energies [ΔU^{DFT}], bond lengths, and bond angles of 4-octyne on fcc and hcp Co (Courtesy: Yan Yang, DiStasio Group)

1.7 Quartz crystal microbalance (QCM) knowledge

QCM has been the powerful approach to monitor the in situ deposition in the science world, like a biosensor [25] and a electrolyte density-viscosity measuring tool [26]. Recently the incorporation with ALD tool has as well been widely applied to observe the real-time mass change at the surface at every exposure step. The results could be utilized as the evidence for a proposed mechanism of the microscopic transportation, such as adsorption/desorption and elimination of ligands [27–30].

The measurement is based on the piezoelectric effect of a specifically shaped AT cut quartz crystal. The following information is well elaborated from the INFICON STM-2 Operating Manual. The crystal will resonate and vibrate at a discrete frequency under a given voltage across the crystal. The displacement at the lowest frequency is parallel to the major crystal face and it is called the fundamental mode while there are anharmonics and third quasiharmonic modes at higher frequencies. Once there is a foreign mass, even a minute one, adhered firmly to the crystal, the frequency at resonance will decrease and it could be quantified as Sauerbrey equation [31] (Eq. 5) while the frequency shift is smaller than $0.02F_q$ Hz. The film thickness could further be calculated under the assumption of a homogeneous film (Eq. 6). For

more precise measurement and higher frequency change, period measurement technique with an additional reference crystal is utilized to accommodate the monitoring under digital time [32] (valid to $0.05F_q$ Hz) and Z-match™ technique considers the acoustic properties which improves the accuracy to $0.4F_q$ under a given film species [33].

$$\Delta F = -\frac{2F_q^2}{A\left(d_q\mu_q\right)^{0.5}}\,\Delta m \tag{5}$$

$$T_f = -\frac{N_{AT}d_q}{F_q^2 d_f}\,\Delta F \tag{6}$$

where

A	: piezoelectrically active crystal area	(cm^2)
d_f	: density of the assumed deposited film	($g\text{-}cm^{-3}$)
d_q	: density of quartz	($g\text{-}cm^{-3}$)
F_q	: the frequency of the uncoated quartz crystal	(Hz)
N_{AT}	: frequency constant of AT cut quartz = 166100 Hz-cm	(Hz-cm)
T_f	: thickness of deposited film	(cm)
ΔF	: the change in frequency of uncoated and coated crystal	(Hz)
Δm	: mass of deposited film	(g)
μ_q	: shear modulus of quartz	($g\text{-}cm^{-1}\text{-}s^{-2}$)

Since QCM is a very sensitive technique, there are various effects that could lead to misinterpretations for the real chemistry from the apparent mass change. The stability of the physical setup are indispensable as well. For instance, the housing and the spring contacts for holding the crystal should not be overstressed or excessively loose and thus the set should be

checked regularly. The crystals that are used under an ALD process are specifically designed to be operated at a higher temperature (i.e. higher than room temperature) within a tolerance range to avoid the intrinsic frequency error. The details could be referred to the catalog of INFICON Quartz Crystals. Another substantial effect is the temperature effect. There are plenty of experimental conditions in an ALD process that could show impact on the equilibrated or transient temperature of the crystal environment, which further manifests as the apparent mass change. Data analysis should take into account the effects from the physical properties like the viscosity and density of the bulk fluid in a hot wall reactor. As shown in Fig. 1-6, different probing gases would cause different extents of variation and different heating profile along the reactor (COLD, TUNED and HOT) affects the apparent mass significantly as well [34]. Regarding removing a general effect in equilibrated temperature, a study showed that the baseline subtraction could be employed during the numeric analysis for compensation [27].

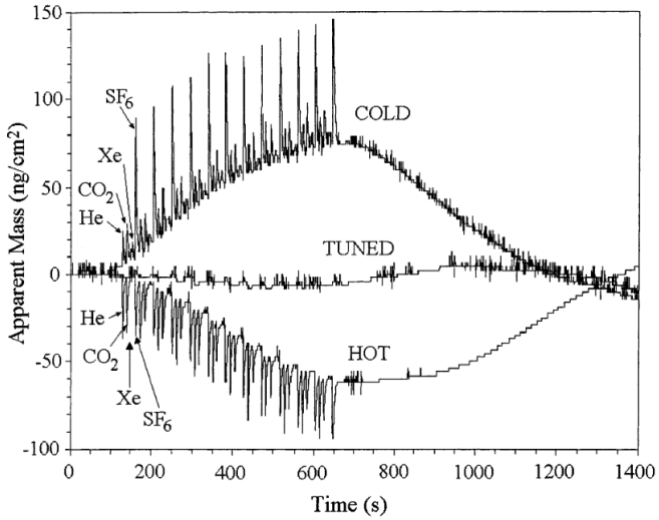

Figure 1-6 Apparent mass change during 48 probe gas pulses (12 cycles of 1s exposure of He, CO_2, Xe and SF_6 followed by 10s purging each) under COLD, TUNE and HOT temperature profile

1.8 Overview of Thesis

The work covered in this thesis has aimed at the area-selective deposition of metal oxide on the silica substrate exclusively with the presence of copper or cobalt substrates. With the support of DFT calculation, 4-octyne is the best candidate as co-adsorbate, which is foreseen to compete for adsorption sites on metal, rehybridize as an intermediate blocking species and desorb without altering the surface. Process parameters have been studied extensively as well to fulfill a successful selective growth within an ALD/CVD window. Tuning of the variables will be essential to produce a high-performance film, such as the dielectric constant for a high-κ oxide, as the future work. The in situ XPS analysis minimizes the sample contamination and characterizes the thin film composition. The real-time QCM technique shows the instantaneous responses at the surface and thus could further induce more understanding of the reaction mechanism while the deposition undergoes. This concept of DoD selective deposition could be exploited into the real-world manufacturing process to reach higher throughput once this study is well developed and could be adopted by the state-of-the-art deposition tools. Future work could potentially expand to other types of selectivity (e.g., DoM, SoS, etc), various substrate species and film types when it comes to different functionality in a transistor, combinations of co-adsorbate and precursor for better effectiveness, and so on.

2. Experimental setup and techniques

2.1 Materials

Materials included in this work have been used to investigate the area-selective deposition with the introduction of co-adsorbate into a typical ALD or CVD process. We have focused on ZrO_x and HfO_x film deposition on metal and native oxide surfaces. The transition metal precursors used in this work are tetrakis(ethylmethylamido)zirconium (IV), $Zr[N(CH_3)(C_2H_5)]_4$ and tetrakis(ethylmethylamido)hafnium (IV), $Hf[N(CH_3)(C_2H_5)]_4$. They are also known as TEMAZ (99.9999%, Air Liquide) and TEMAHf (99.9999%, Air Liquide). Metal amides have been reported to have metal-nitrogen bonds that are susceptible to reaction on hydroxylated surface (native oxide on silica) and their intrinsic thermal stability and sufficient vapor pressure make them ideal candidates for gas-phase oxide thin film deposition [4]. The vapor pressure of TEMAZ and TEMAHf under different temperature is shown in Fig. 2-1. The structure of the two precursors is shown in Fig. 2-2, while the central dark-grey atom is Hf in TEMAHf and it is Zr in TEMAZ.

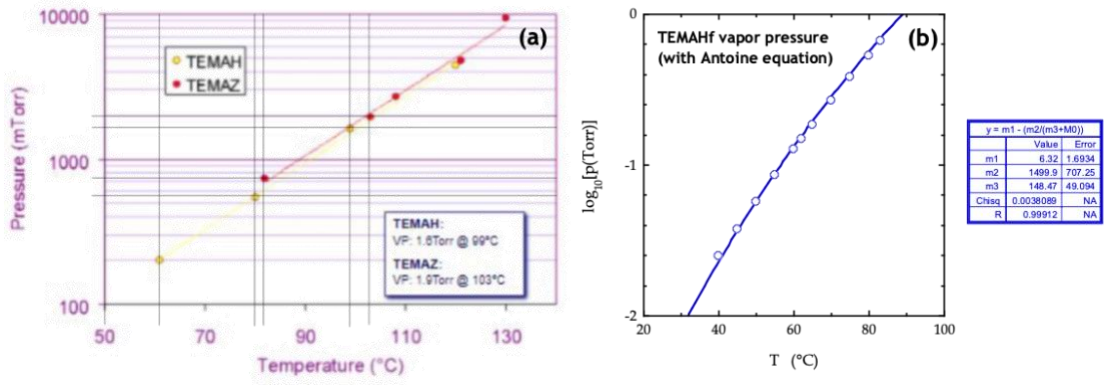

Figure 2-1 (a) The plot of the logarithm of TEMAZ and TEMAHf partial pressure to temperature (provided by Air Liquide) (b) The partial pressure of TEMAHf data fitted by Antoine equation (courtesy to Prof. James R. Engstrom)

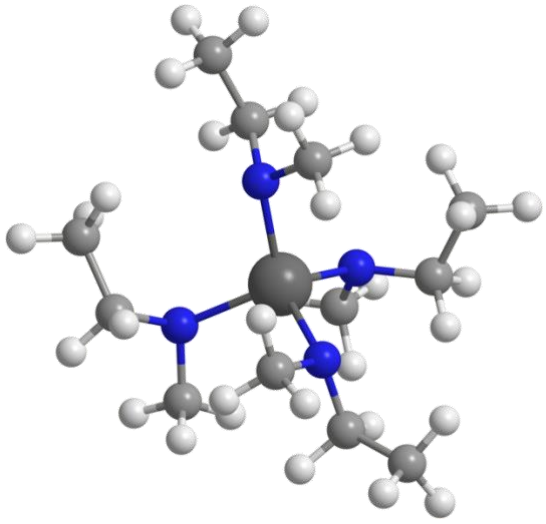

Figure 2-2 Structure of TEMAHf and TEMAZ (courtesy to previous group members)

The co-reactants in this work are molecular oxygen (O_2, UHP 99.99%, Airgas) as cylinder and DI water (ultrapure H_2O, ELGA Labwater, acknowledgement to Daniel Research Group). 4-octyne (99%, Sigma-Aldrich) is chosen as the introduced co-adsorbate. The structure

of it is shown in Fig. 2-3. All the liquid-phase chemicals mentioned above are all prepared in stainless steel bubblers in a glove box (acknowledgement to Cornell Center for Material Research, CCMR) to avoid air exposure.

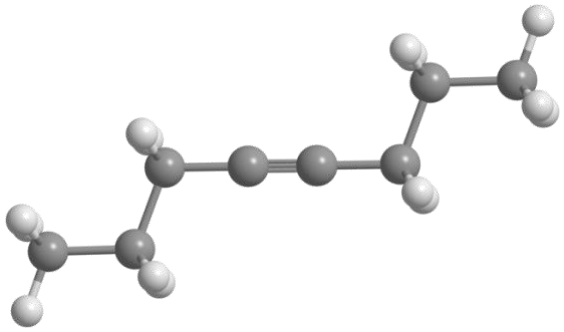

Figure 2-3 Structure of 4-octyne (courtesy to previous members)

2.2 Micro-reactor/UHV system

The Micro-reactor /UHV system is a custom-designed multiple-stage system that is capable of loading samples, conducting thin film deposition and in situ surface analysis with XPS. Most of the experiments discussed in this thesis are performed in this system. Some of the coupon samples from QCM system were loaded to this system and analyzed with XPS.

The system consists of 4 major sections for respective purposes: a load-lock chamber, an intermediate chamber, a micro-reactor chamber and a main analysis chamber with various characterization tools (shown in Fig. 2-4). They could be isolated from or connected to the adjacent one by the corresponding gate valves. As principle, any of the volume should be continuously pumped over a long time period (to avoid leaving a “dead volume”). The samples

are transported among the chambers via sample manipulator for different processes. For the most common routine, after the coupon samples are placed onto the sample holder, it is loaded to the transfer arm in the load lock chamber. After it is pumped down sufficiently with a turbomolecular pump, we could open load lock gate valve and transfer the sample holder from transfer arm to the sample manipulator located in the intermediate chamber. By controlling the sample manipulator, we could transport the sample holder among different positions. With micro-reactor chamber connected to intermediate chamber, we could perform a deposition experiment. After sufficient pumping down, we could transfer it down for analysis with intermediate connected to main surface analysis chamber. For different objective and analysis, the system is a very powerful tool to fulfill a comprehensive study without samples being exposed to air.

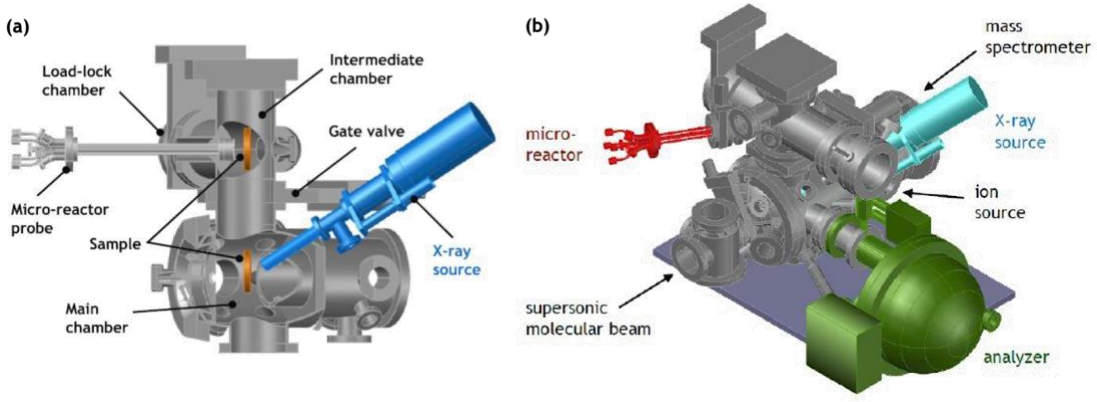

Figure 2-4 (a) Schematic of the three chambers (load-lock, intermediate and main analysis chambers) and the micro-reactor probe (b) Schematic of all the characterization tools mounted on the main analysis chamber

The custom-designed molybdenum (Mo) sample holder is shown in Fig. 2-13. The 2-slit holder (two 10×25 mm^2 rectangular spots) enable us to observe the results for two different substrates under the same experimental conditions. After the coupon samples have been placed in the recesses, the cap plate is then placed on and fixed with three fingers (120° apart). On the circumference of the sample holder, three of the recesses are used for the locking mechanism for fingers on transfer arm while the other three are for those on sample manipulator. The recess has a free end and dead end. The transferring between transfer arm and sample manipulator is done by anti-clockwise and clockwise rotation to make fingers locked to dead end while the ones from the counterpart are unlocked to free end. The metal sample holder contacting the grounded chamber system also reduces charging effect on the samples while doing an XPS experiment.

The sample manipulator (Thermionics SMR-3, Thermionics Northwest, Port Townsend, WA) plays an important part in transferring samples. It allows three dimensional axial movements (i.e., x, y and z), polar rotation (θ) and also in-plane rotation (azimuthal). The polar translation movement requires differential pumping, which is achieved by an additional ion pump (Ion Pak 200, Perkin-Elmer Products, Waltham, MA) to pump out the intermediate volume separated by O-rings and Teflon seals. On the back of the manipulator, there is a pyrolytic boron nitride heating element incorporated with a heating power controller and a temperature reader. Based on the temperature calibration from previous members (using thermocouple sticked to the sample surface, measuring the surface temperature and fitting it as a polynomial function based on the heating power/temperature reading), we could adjust the heating power according to the desired substrate temperature accurately.

Pressure is the key indication of a UHV system. Most of our action, judgement or even fault analysis depend heavily on the pressure reading. There are three types of pressure reading tools that are used in this system. First, the thermocouple gauges are mainly used to measure the low-vacuum pressure (around 10^{-2} Torr), which are located at the fore-line of the six mechanical pumps (mostly rotary vane pumps) used in this system. The working principle is that based on the thermal conductivity of the amount of gas molecules present in the sensor tube (the pressure in the tube), the temperature of the heated filament at a fixed current is then measured by the thermocouple, which could be converted to a pressure reading. Secondly, a Baratron® (mks 627D) located on the delivery line is used to measure the real reactor pressure (insensitive to gas type compared to the other two types of tools). The working principle is that by measuring the capacitance of a radially tensioned diaphragm with the high-vacuum reference side, it is converted to a digital signal (sensor range in voltage) that is proportional to the pressure (full scale in pressure). Ion gauges are a common high-vacuum pressure-measuring tool. They are used for detecting the UHV pressures of load lock and main analysis chambers in this system. Gas molecules are ionized by the heated filament and captured via high electrical field by the cage surrounding the filament. The detected current is then converted to a pressure reading. Its working condition should be below 10^{-6} Torr or else the filament/cage would be burnt off due to the high current.

The load lock chamber is used to reduce the cycle time and UHV volume exposed to ambient air condition. The interlock system (designed by previous members), including an isolation valve, a backup pump (mechanical pump), a pneumatic valve for venting gas and a turbomolecular pump (Pfeiffer TMU 071 P), is triggered by the turbomolecular pump power supply unit (PSU). Once the volume is isolated from intermediate chamber and the power is off ,

the isolation valve will shut off and the turbomolecular pump will begin to spin down. As long as the rotation speed has reached 600 Hz, the pneumatic valve will open and start to flow N_2 into load lock to pressurize the volume. The design is to prevent backflow of air into the volume and expedite the venting process; meanwhile, it is a safety system for unexpected power outage events. We could then swap the samples and re-lock the sample holder onto the transfer arm. It is crucial to keep the inner surface free of contamination, i.e., skin oil (hydrocarbon); thus, the performer is required to wear nitrile gloves during the whole process and wipe down the surface with beta wipe and acetone afterward. The sealing of the load lock door is important as well. The O-ring in the groove should be positioned firmly and re-greased with vacuum grease after a certain time to create the high vacuum condition. After the door is latched, we could then power the controller and start the pump-down process (vice versa for the interlock system, except the venting valve will close once it is powered). We should expect the pressure to be around $10^{-6} \sim 10^{-7}$ Torr over 3 hours.

The intermediate chamber is mainly used as the deposition reaction space. As mentioned above, it is the only chamber that is not directly connected to any of the pump; thus, there should be one gate valve open during most of the time (i.e., open only load lock gate valve, reactor gate valve or main gate valve to make it connected to the corresponding chamber). Once the pressure of load lock is low enough and since normally the intermediate chamber is under UHV, we could transfer the sample from the transfer arm to the sample manipulator in the intermediate volume. To perform the sample annealing (discussed in Chapter 4.2), we could consider the process to be under an environment with flow or no flow. There are pros and cons for the respective procedure. With a flow, the flow over the sample surfaces could be served as a “blanket” to them. The escaped species from surface are more easily brought away and at the

same time protected them from reactive species by the convection. However, vice versa, if the flow is not an ultra-pure inert gas or the background of reactants is high, the surface is more susceptible to reaction with the contaminants. The chamber status will then be intermediate connected to micro-reactor chamber since the volume with a flow should be pumped by a mechanical pump (being directly pumped by E2M30, Edwards), and should never be pumped by a turbomolecular pump. As for annealing without a flow, there is no so-called a protection layer and it is less efficient to bring away the escaped species under comparison. Thus, while we do annealing without flow, we would do it under UHV to suppress the potential reactants. The intermediate chamber is then connected to main analysis chamber.

To connect intermediate (under UHV, ~10^{-8} Torr) to micro-reactor (under low vacuum, ~10^{-2} Torr) volume, the critical part is to pressurize the high vacuum volume first. Since if we directly them together, the pressure at E2M30 will turn out to be the higher one and there will be a backflow into the system. This is absolutely an unwanted situation since the hydrocarbon content (pump oil vapor) in the system will rise and thus get contaminated. Consequently, the intermediate chamber should be isolated from all other chambers (forming a dead volume) and pressurized with an independent flow line. Then, we could open reactor gate valve to pump on the volume by E2M30. In the other case, we will connect the intermediate to main analysis chamber. The pressure difference between these two is not as high as that, but it still could pose a force on the main gate valve normally or overload the three turbomolecular pumps that are pumping on the main analysis chamber (Source: Seiko Seiki STP-310CB1 / Ante: Pfeiffer TPU 261 PC / Main: Osaka TG 403M). To make the pressures comparable and open main gate valve manually, we use a bypass valve to leak gas into main analysis chamber by controlling the openness and monitoring the fore-line pressure.

There are several characterization tools, which require an UHV working condition, mounted on the main analysis chamber. Typically, we could conduct ion sputtering with ion source (SPECS, PU-IQE 12/38, Berlin, Germany), gas analysis with quadruple mass spectrometer (QMS, Hidden 3F/EPIC, Hiden Analytical, Warrington, UK) or molecular beam mass spectrometry and post-exposure surface analysis with XPS (Omicron DAR 400 X-ray, Taunusstein, Germany) or low-energy ion scattering spectrometer (LEISS, Omicron EA 125, Taunusstein, Germany). Sputtering is a technique for removing surface metal compounds, mostly oxides and carbides, in order to yield a clean metal surface. It is a more destructive way, which induces physical ion bombardment and chemical reaction with radicals, compared with an annealing process. The ion source generates ion beam with argon or helium introduced into main chamber (through an independent delivery line) and it rasters the designated area. The ion beam is deflected by two orthogonal electrostatic fields with an adjustable duration per dot successively. The results will be discussed in Ch. 4.1.1 regarding cobalt surface cleaning. We could perform two kinds of gas analysis with QMS: a Residual Gas Analysis (RGA) and a Multiple Ion Detection scan (MID). The principle is detecting the intensity of the ionized and fragmented gas molecules based on the mass-to-charge ratio (m/z). The technique is mainly used to examine the condition of the vacuum system. RGA sweeps from m/z = 1 to 300 and is usually conducted to identify an unknown contaminant lingering in the system or typically after a system venting/pumping-down process. A feature of RGA results of a vacuum system is that there are consecutively decreasing peaks with an offset of 14, which originated from the backflow of pumping oil (hydrocarbon consists of CH_2 whose mass is 14 as the smallest fragment). MID scan is programed to pick up specific m/z values in loop continuously as the time goes. MID scan could be served as a background check or an isolation testing for a fully shut-off valve. Intensities for H_2O (m/z=18), N fragment (m/z=14) and O_2 (m/z=32) are typical

indicators for a leak or an unwanted gas accumulation (virtual leak or clogging) in the system. He (m/z=4) signal is an indicator during a helium leak check. By squirting helium directly to test ports at a fitting or along the surface, we could know the exact leak location if strong signals appear.

For the maintenance of the vacuum system, since water vapor in the ambient air has strong tendency to adsorb on stainless steel walls, we will have to bake all the corresponding sections of the system once the inner wall has been atmospheric after an venting process (intentionally or unexpectedly). Baking process involves heating elements and aluminum foil covering the compartments on the air side to be heated up. Flows will be introduced or at least the volume is to be pumped to expel the water vapor for 0.5-3 days based on the extent of the exposure and pressure behavior.

2.2.1 Chemical delivery system

Chemical delivery is an essential real-life engineering design to be dealt with besides the microscopic reaction condition we are looking into. Only if the reactants reach the reaction zone could we further discuss the chemical behavior. There are several procedures and modifications that the previous members have done to ensure an ideal chemical delivery to the reaction zone. Instead of delivering the chemicals with fixed hardware system, they (Taewon Suh as the leader) have designed the sliding panels to reduce the delivery distance. The point is that with excessive delivery length, we would expect a significant time delay between turning on the carrier flow and the reactants actually entering the reactor. Additionally, for a line that is used to deliver sticking species, like the precursor or co-adsorbate in this study, the so-called

line passivation is a non-trivial step before conducting an experiment. Line passivation usually takes a duration of ten times longer than the exposure time in a typical deposition experiment to ensure the chemical is not considerably consumed during delivering. Thus, a minimized length of delivery line is preferable and, in our case, we have been using flexible tubes as bridges between the sliding delivery panels and the fixed sections (i.e., gas cylinders and reactor lines mounted on the translational motor, which would be discussed in next section) so that the panels are movable with the translational motor without severe strain on the tubes.

The delivery system consists of three panels (named as A, B and C panel) on the sliding trail, which are used for delivering co-adsorbate, co-reactant and precursor respectively. The assembly mounted on a single panel is shown in Fig. 2-5 and is similar on all three panels. The top line is used for flowing purge gas (called purge line) while the lower one is used for delivering reactants (called carrier line). The storage is typically a bubbler for liquid-phase reactants or a gas cylinder directly connected to carrier line if it is a gas-phase reactant. The bubbler is designed as an enclosed volume with a dip tube as inlet and an outlet tube as the only way out. When the carrier flow flows into the bubbler, it will bubble through the liquid and ideally reaches vapor-liquid equilibrium to carry out the gas-phase reactant. The carrier flow rate is one of the parameters to determine the concentration (partial pressure) of the reactant in the flow. High flow rate could carry out more molecules with higher momentum but, at the same time, the residence time in the bubbler might not be enough to reach vapor-liquid equilibrium. To control the flow rate, mass flow rate controllers (MFC, mks instruments, Andover, MA) are mounted on all six lines at the downstream of the respective cylinder regulator. They measure the heat capacity of the gas in a bypass sensor tube to determine the mass flow rate (standard cubic centimeters per minute, sccm, as unit). Manual quarter-turn diaphragm valves (Swagelok,

Solon, OH) are used for several purposes, like minimizing atmospheric exposure, directing flows through bubbler, etc. Six three-way pneumatic valves (Fujikin, Osaka, Japan) are used to direct flows in each line to either micro-reactor or E2M30 (mechanical pump), which is controlled by sending signals to solenoid valves to flow compressed air into the pneumatic valves or not (depending on whether it is a normally closed or normally open valve switching to what status). The automated system is executed by using LabVIEW program to control MFCs, twelve pneumatic valves (six three-way pneumatic valves) and a PID pressure controller (be discussed on next section) for various experimental objectives. Details will be discussed in the following contents.

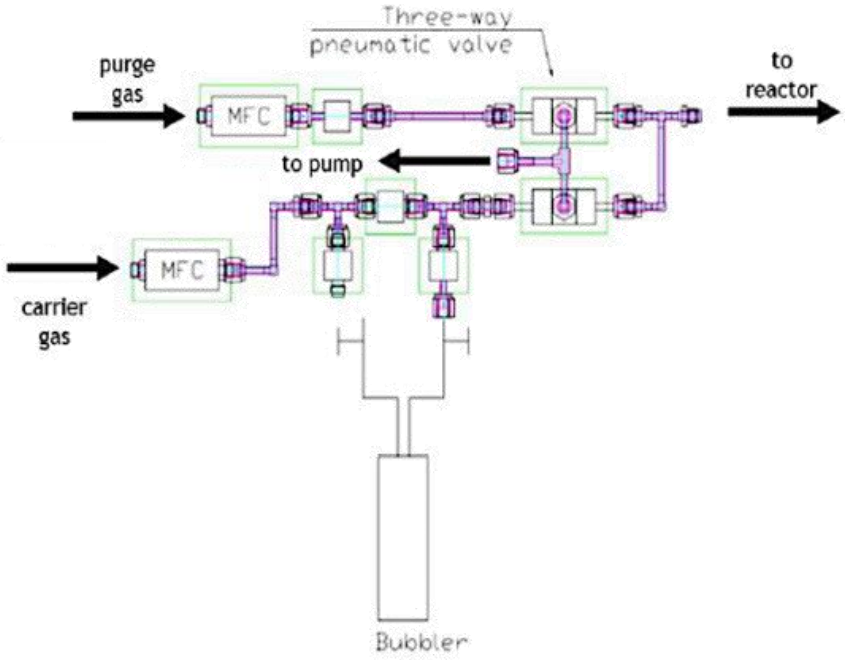

Figure 2-5 AutoCAD drawing of components on a single delivery panel with indications for flow direction (courtesy to Taewon Suh)

In early 2021, we observed an unwanted spatial variance in flow dynamic (i.e., the deposition thickness was different on the left and right samples using same substrate species) with the lines from A, B and C panels were connected to the fluidic feedthroughs spatially in sequence on the horizontal view plane indicated in Fig. 2-7 (a). Consequently, we had altered our chemical delivery manifolds so that the two lines with greater partial pressure change during delivering , A and C lines, are connected to the ½" central tube while B line was split in two with a tee and connected to the two ¼" tubes on both sides. To test whether there was a symmetrical chemical delivery, we performed a ZrO_x CVD with 4-octyne experiment (4-octyne carried through A line, O_2 flow through B line and TEMAZ carried through C line) on both silica samples. We then performed an XPS line scan (discussed in Ch. 2.2.4.3 and the six sampling points are shown in Fig. 2-13) and the thin film growth on both samples was close to uniform within the reaction zone range. The results are shown in Fig. 2-6. To optimize the gas-phase reaction environment, we plan to mount an additional ¼" fluidic feedthrough in the ½" central tube for flows from C. In this case, A and C flows would be separated and the gas-phase interaction would be minimized. This is a future work to be done.

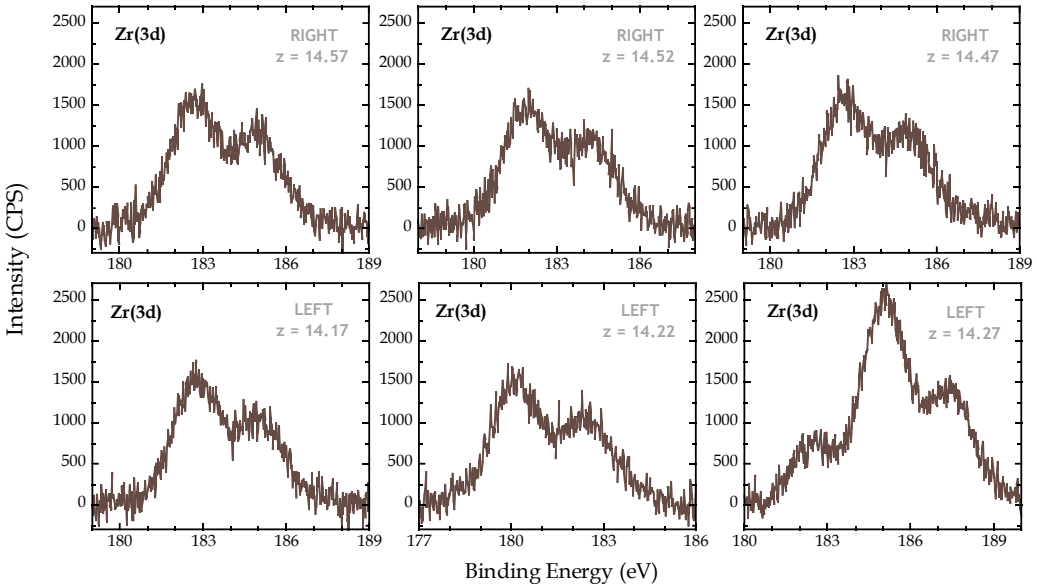

Figure 2-6 XP spectra for Zr(3d) region at the six sampling points for line scan analysis to inspect the uniformity of chemical delivery

2.2.2 Micro-reactor and reaction zone

The micro-reactor in 312 system, in which the deposition experiments were conducted under low-vacuum (~ 10 Torr), is an innovative design that is in coordination with the UHV system. The micro-reactor consists of a translational micro-reactor head, the sample holder and flowing the so-called “curtain flow” to form an ideal confinement. Previous members (Jiun-Ruey Chen as the leader) have designed it by computational fluid dynamics (CFD) with COMSOL® and thus it establishes the use of curtain flow (more elaborated details are in his thesis). The whole assembly is shown in Fig. 2-7. On the air side, the gas inlets are connected to the delivery manifold. The flange is mounted to a translational motor and the vacuum side (fluidic feedthrough and micro-reactor head) is inside a bellow. The exhaust ports are connected

to E2M30 and thus the volume covered by the bellow is continuously pumped by it. On the other end of the micro-reactor chamber is the reactor gate valve, which isolates itself from the intermediate chamber. After pressurizing the intermediate chamber and opening the reactor gate valve, the micro-reactor head is moved in to approach the sample holder (on the sample manipulator) located in the intermediate chamber. The precise stop point is determined by inspecting the electrical continuity among the four electrical probes connecting to the respective spring-loaded probes on the micro-reactor head. The gap should be around 0.05-1 cm. Once at least three probes form an firm touching with the sample holder and are showing single-digit resistance from a multimeter, it is believed that the micro-reactor head is close enough to the sample holder. The two semicircle effluent groves on the micro-reactor head play vital parts in determining the flow dynamics; i.e., the residual species from reaction zone flows eccentrically and the species from curtain flow transports concentrically.

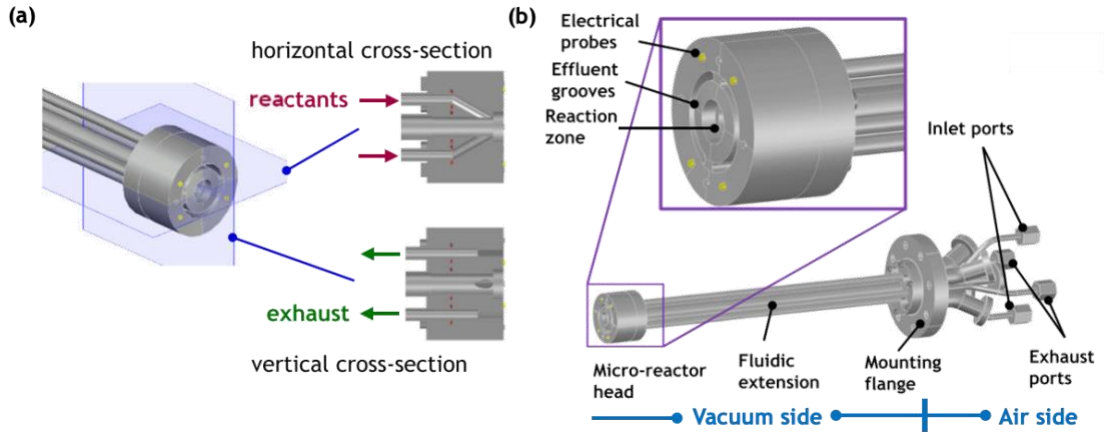

Figure 2-7 (a) Schematic of the cross sections indicating the feed lines and the exhaust lines (b) Schematic drawings of the translational micro-reactor assembly.

Nitrogen has been used as the curtain flow in this study. The ratio of the total flow rate from the chemical delivery system to the curtain flow rate is a vital parameter to be adjusted as well. However, we have seen long transient during the pumping down of the micro-reactor. It could either be the low conductance of the effluent grooves or there is a leak of the chemicals through the gap into the intermediate chamber; thus, it leaves a larger pumping volume entailing a longer pumping time. Besides using the electrical check to ensure the physical confinement of reactor zone, we have planned to try with hexafluoroethane (C_2F_6, 98%, Sigma-Aldrich) as a candidate for curtain gas. Generally, it is inert under ambient and is mostly used as a refrigerant. In semiconductor industry, C_2F_6 plasma is used as a cleaning gas for the chamber. In our case, we will test out whether a better confinement could be achieved by utilizing such a heavy gas species. We expect a lower diffusivity (D) from a heavier molecule at low density and also the higher momentum could prevent the inner chemicals from leaking eccentrically. The equation for diffusivity approximation, based on Chapman-Enskog kinetic theory and ideal gas law, is written as Eq. 7 [35].

$$D = 0.0018583\sqrt{T^3\left(\frac{1}{M_A}+\frac{1}{M_B}\right)}\ \frac{1}{p\,\sigma_{AB}\,\Omega_{D,\,AB}} \tag{7}$$

where

D	: diffusivity	(cm^2/s)
T	: temperature	(K)
M_x	: the molar mass of species x	($g\text{-}mole^{-1}$)
p	: pressure	(atm)
σ_{AB}	: the distance at which Lennard-Jones potential between A and B is zero	(Å)
$\Omega_{D,\,AB}$	: the collision integral for diffusion	(-)

The effectiveness of using C_2F_6 as curtain flow had been investigated. Based on the results from the initial studies, the modification could have worked as we expected but it might not be significant. We had conducted 5 cycles of pristine HfO_2 ALD and HfO_2 ALD with 4-octyne under N_2 and C_2F_6 as curtain flow respectively. The deposited film is supposed to be comparable between pristine ALD and ALD with 4-octyne since 4-octyne should not participate in the deposition reaction. As shown in. Fig. 2-8, although it did not show selectivity with 4-octyne, the deposition was more comparable between with and without 4-octyne under C_2F_6 as curtain flow. Possible explanation is that the high partial pressure during 4-octyne exposure might had undermined the confinement when using N_2 as curtain flow and thus there was less reactants for deposition due to leaking. The issue might have been mitigated by using C_2F_6 as curtain flow.

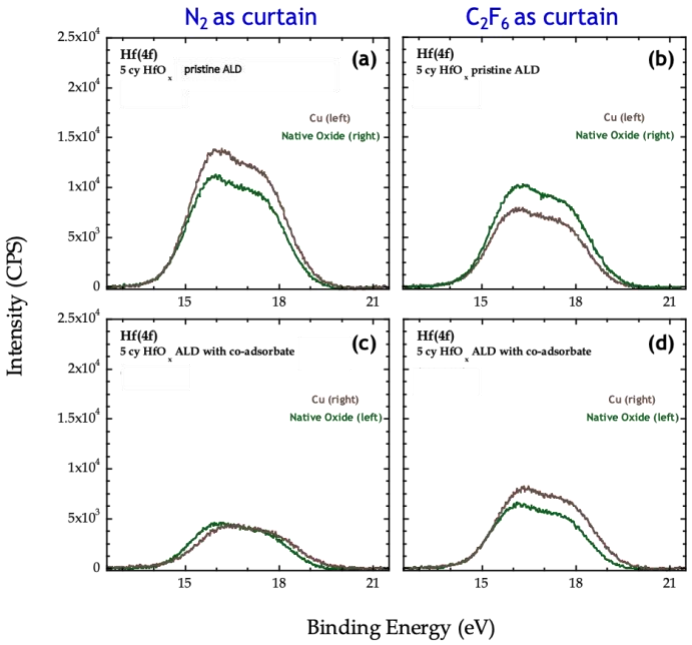

Figure 2-8 XP spectra for Hf(4f) region from 5 cycles HfO_2 (a) pristine ALD with N_2 as curtain flow (b) pristine ALD with C_2F_6 as curtain flow (c) ALD with 4-octyne and N_2 as curtain flow (d) ALD with 4-octyne and C_2F_6 as curtain flow

The dimension of the reaction zone on the sample holder plane is tested with CFD model [36] and is shown in Fig. 2-9. And thus, based on the calibrated z-position, we could depict the reaction zone with an XPS line scan after an deposition experiment. Moreover, we could have the information of the confinement as well based on the film deposition beyond the reaction zone. In some cases, visual check for a "stain" (looks like the periphery of the red-shaded area on each sample in Fig. 2-9 (a)) after a thick deposition could help with the alignment between the micro-reactor head sample holder. More details would be discussed in Ch. 2.2.4.3.

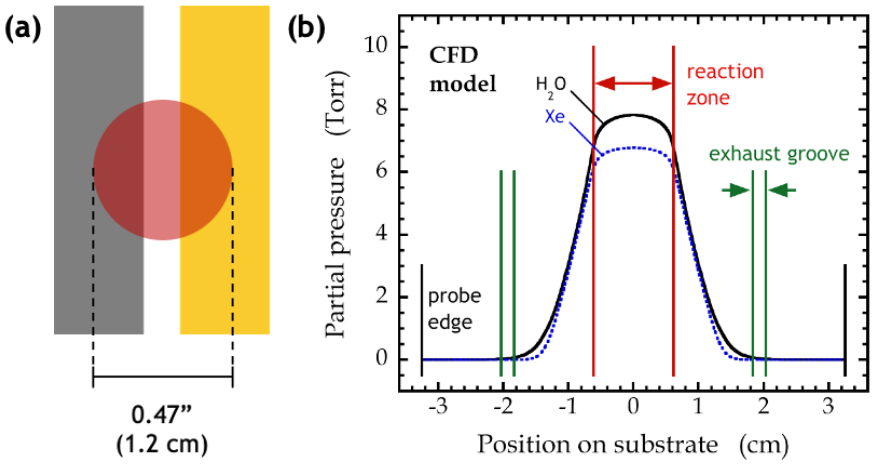

Figure 2-9 (a) Schematic of the reaction zone projected onto the two coupon samples on the sample holder (shown as the red-shaded region) (b) Partial pressure of H_2O and Xe as a function of position on the sample surface as predicted by the CFD model. The reaction zone is thus the region where it shows the maximum partial pressure of reactants

2.2.3 Mixing in reaction zone

The pressure at the microreactor is estimated by Baratron located roughly at the upstream of the sample surface by 22" on the ½" central delivery tube with the assumption of low pressure drop. As discussed in Ch. 2.2.1, the alteration of the manifolds makes flows from A and C go through the central tube. Since it is crucial to have the chemicals be well-mixed before the exposure to sample surfaces (a symmetrical delivery), we should aim for a longer mixing length in the cylindrical volume. The characteristic mixing length is proportional to $\sqrt{D \times \tau}$, where D is diffusivity [=] cm^2/s and τ is residence time in the cylindrical reaction zone [=] s. Generally, mass flow rate is well-controlled by the MFCs; thus, the condition at fixed mass flow rates could be discussed in the following.

At fixed mass flow rates, τ is proportional to the pressure based on ideal gas relation and fixed reaction zone; while D scales with the inverse of the pressure based on Eq. 7. Thus, theoretically, the mixing length should be independent of pressure since it is cancelled out. On the other hand, mixing length scales with the inverse of the square root of mass flow rate due to τ; thus, for a better mixing, lower total flows from the panel could be the guideline (curtain flow in our case does not affect much to the reaction zone under perfect confinement). Besides the mixing length, a less dominant factor is that at high pressure, the volumetric flow rate is lower at fixed mass flow rate; in the meanwhile, the volume of gas-confined reaction zone ideally should be smaller. It could reduce the spatial variance and lead to leaking to some extent.

2.2.4 X-ray photoelectron spectroscopy (XPS)

XPS has the advantages of investigating surface chemistry (within 10 nm) and unveiling the chemical environment of the surface material, i.e., oxidation state of the atom and adjacent atoms. The high energy X-ray photons bombard the surface, excite mostly the core electrons of the atoms and they escape the surface with a sufficient kinetic energy. The energy conservation relation is simply expressed as Eq. 8 [37].

$$E_B = h\upsilon - E_K - \Phi_{spec} \quad (8)$$

where

E_B : binding energy of the electron to the atom (eV)

$h\upsilon$: the energy of photoelectron determined by anode source (eV)

E_K : kinetic energy of the escaped electron (eV)

Φ_{spec} : a constant spectrometer work function (= $E_{vacuum} - E_{Fermi}$) (eV)

The emitted electrons are collected through extraction lenses, detected through a concentric analyzer and then converted into digital signals (intensities). The intensities could be described by Beer's law. That is, the intensity (I) is proportional to $\exp(-d/\lambda)$, where d is the depth of the photoelectron from the surface and λ is the mean free path (describing mostly inelastic scattering, and is related to the thin film material and the initial kinetic energy of the photoelectron). Based on the universal λ and Beer's law, the characteristic analysis depth is often noted as 10 nm where photoelectrons are mostly collected. The analyzer picks up photoelectrons from not only a photoemission process but also an inelastic collision process, like plasmon loss, X-ray satellites (due to multiple and contingent emission of x-ray lines from

non-monochromatized X-ray source), etc. Beside the initial chemical state of the atom, the final state would lead to shakeup, shakeoff (excitation of valence electron by the ejected core electrons) and multiplet splitting (mostly occurs when there is unpaired electrons in valence band); thus, the spectra would sometimes show broadened and multiple peaks feature. The handbook [38], Thermo Scientific XPS Reference Table and NIST XPS Database are good references for us to identify peaks in the spectrum.

There are two modes in XPS analyzer, constant analyzer energy (CAE) and constant retard ratio (CRR), that lead to different background appearance. Since the pass energy is constant in CAE mode, the transmission function is proportional to the inverse of the electron kinetic energy under first approximation; while the transmission function is proportional to the electron kinetic energy in CRR mode. CAE mode is used for survey and detail scans in this work.

Casa XPS software is used to interpret the spectra more accurate. Background removal is important for a quantitative analysis of the intensity area since the background intensities are mostly from inelastic collision that are not from the surface. Moreover, for a transition metal compound, background subtraction is usually not linear and requires accurate models. Shirley background model states that the background scales with the intensity area under the peak [39]. It is a better model for the peaks structure when the slopes before and after the peaks are comparable and is used to reproduce a step between the start and end points [40]. An iterative Shirley background is used in our analysis [41]. A 70% to 30 % mixture of Lorentzian and Gaussian fitting functions respectively are used in the software for the peak intensity raw area. Under the assumption of that adventitious carbon is inevitably adsorbed on the surface and

charge accumulation is the same extent on the sample surface, binding energy calibration for the spectra is conducted by offsetting the whole spectrum based on the shifting of aliphatic carbon peak to 284.6 eV.

Besides the main peaks mentioned above for identifying the elements, Auger peaks are a series of peaks that would be very informative as well for a comprehensive understanding. Auger electrons are excited through core-hole relaxation process and is independent of the initial photon energy. However, the overlap between Auger peaks and main peak will sometimes mislead the analysis. To remedy this issue, the system is equipped with dual anode source, aluminum source at 1486.6 eV and magnesium source at 1253.6 eV, to provide a "shifting" of the Auger peaks for better peak analysis. It is also known that the Auger peaks will shift or reshape stem from different chemical state, which could provide more obvious information besides the main peaks [42].

2.2.4.1 Angle-resolved X-ray photoelectron spectroscopy (ARXPS)

Take-off angle is defined as the angle between the surface normal and the direction from the spot to the analyzer. Signals from large to low take-off angles are collected on the same sample spot for ARXPS studies. At higher take-off angle, the spot size is larger and the collected electrons are mainly from near surface while those from deeper substrate are mostly hindered due to inelastic collisions. With sampling at different take-off angle, the concentration profile of the film layers, interface roughness or the uniformity could be portraited. Several models for signal intensities versus take-off angle with different concentration profile based on Beer's law

are developed by our previous member, Kevin Hughes and are elaborated in his thesis. The summary of the models are shown in Fig. 2-10 [43].

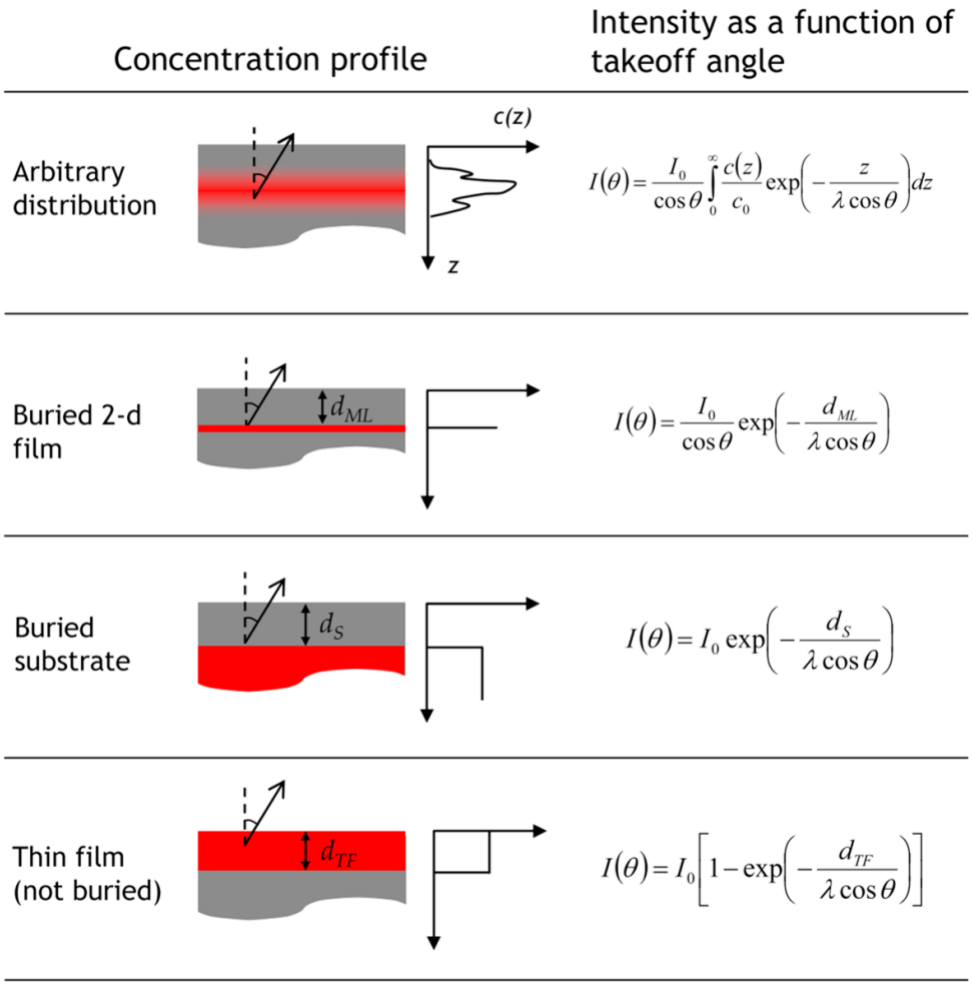

Figure 2-10 Summary of different concentration profile and the corresponding intensity function of take-off angle

Analysis is conducted by plotting the raw intensity areas of the main elements (mostly the substrate, thin film, C 1s and O 1s signals) versus the take-off angles. By fitting the points

based on the models, we could have the value of d/λ where d is the film thickness and λ is the inelastic mean free path based on the film material, which is calculated by QUASES-IMFP-TPP2M software developed by Sven Tougaard (Fig. 2-11). Moreover, based on the R-squared of the fitting, we could evaluate whether the model is suitable or the film characteristics (i.e. roughness, homogeneity of the film, etc) are ideal. One of the results of pristine zirconia ALD on copper sample are shown in Fig. 2-12. Zr 3d 5/2 data fits the thin film model while Cu 2p 3/2 data fits the buried substrate model well. C 1s and O 1s does not fit well with any model and it might due to the homogeneity of the element. Adventitious carbon might be incorporated into the film while oxygen exists in the film due to co-reactant or the residual copper oxide at the interface.

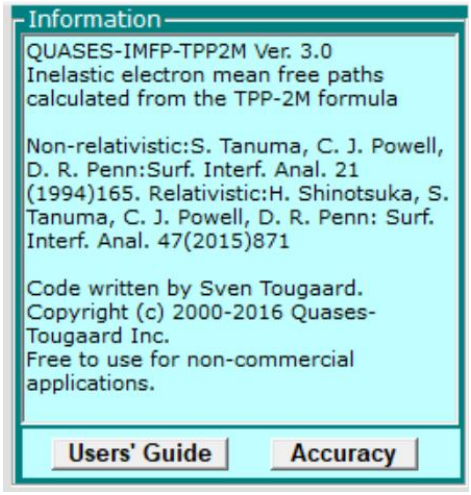

Figure 2-11 Information of QUASES-IMFP-TPP2M software for inelastic mean free path calculation

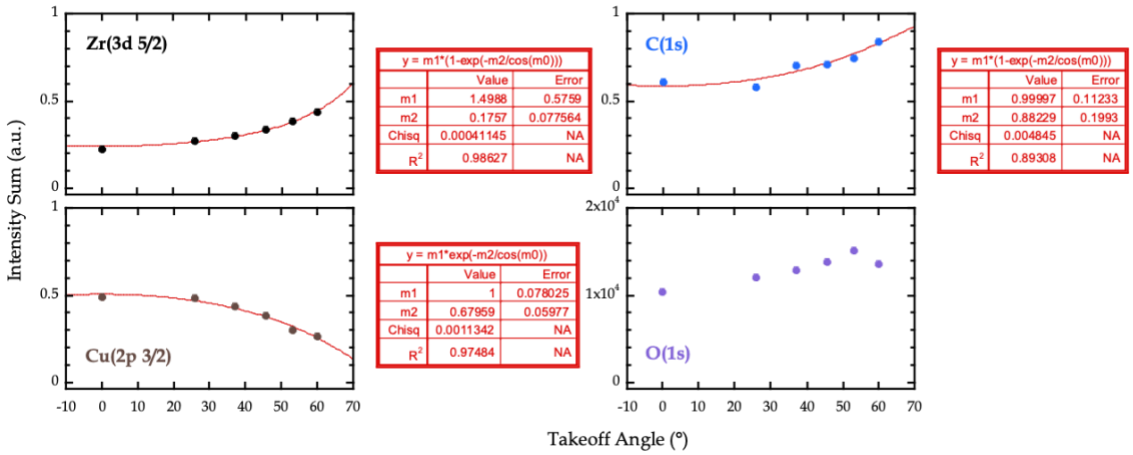

Figure 2-12 Summary of the analysis of ARXPS for pristine ZrO_2 ALD on copper sample

2.2.4.2 Thickness calculation

Besides estimating the thin film thickness from ARXPS study, the thin film thickness can be calculated directly by using a reference intensity with the buried substrate and thin film models described in Fig. 2-10. For the former one, the intensity of a clean surface (annealed Cu, Co and silica samples in our case) is used as the reference. As for the latter one, the intensity of a semi-infinite film is used as the reference. A film will be called as semi-infinite film when the substrate signals have been fully attenuated and not been observed. Consequently, the film should be at least 10 nm, which is the limitation for XPS to pick up the signals.

2.2.4.3 Line scan analysis

Line scan is a simple technique that utilize both XPS and sample manipulation. At a fixed take-off angle (0° in our study), we change azimuthal and z to do XPS at the sampling spots over the samples and sample holder for specific purposes. As shown in Fig. 2-13, a line scan analysis for post-exposure samples could depict the reaction zone (red-shaded area) or observe the uniformity of the film deposition based on the intensity area of the feature peaks. In our recent case, the calibrated z center point is 14.37. Since the spot size is 1200 μm in diameter (~ 0.047”), we sampled the spots with a discrepancy of 0.05” for closer study (moderate overlapping). Secondly, for a more baseline study, by placing two identical clean substrates on the sample holder, the line scan analysis could inform us of whether the calibrated analyzing position is correct (accuracy is undermined due to the spot size). An result is shown in Fig. 2-14 for the short-side analysis (azimuthal as shown in graph and varying z position, shown in Fig. 2-13), which is done on two clean copper substrates where Zr 3d signals are from the deposited residual over time on the sample holder. The results roughly match with the dimensions (Zr signal is high and Cu signal is low on the sample holder, vice versa) and thus we could trust our calibrated central z position.

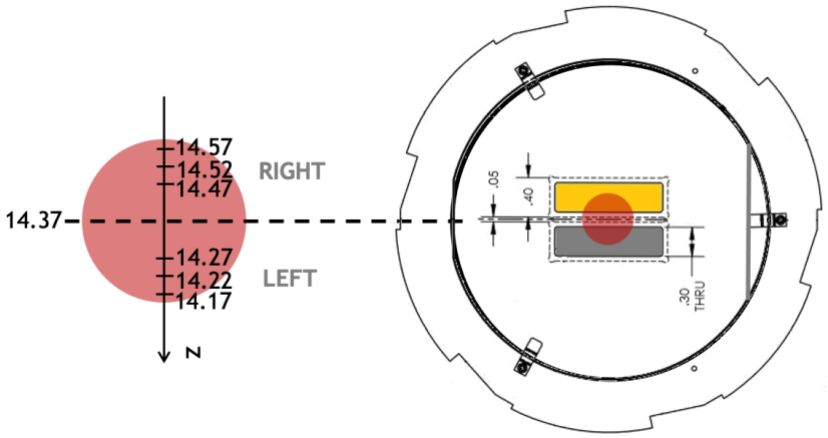

Figure 2-13 Schematic of the 2-slit sample holder and an example of sampling points

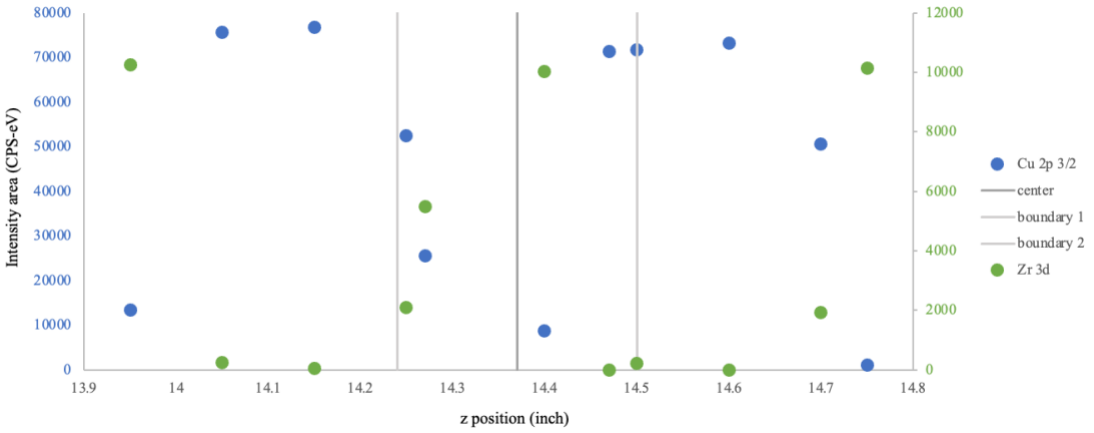

Figure 2-14 Summary of a line scan analysis with the intensity area of Cu(2p 3/2) and Zr(3d) versus z position

3. Computational work

3.1 Surface coverage simulation

Since competitive adsorption of co-adsorbate is important in this study, I have collaborated with Prof. Robert A. DiStasio Jr. and Yan Yang on a rudimental script for surface coverage simulation by Python. The strategy described here focuses on simulated annealing (SA) under a series of fictitious temperatures with an adjustable cooling rate (CR). By randomly choosing a site and flipping the occupation number (1 represents occupied/adsorbed while 0 represents unoccupied), the move is accepted by Metropolis Monte Carlo method. The scheme is that if the energy change is negative (downhill), the move is always accepted and while if the energy change is zero or positive (uphill), the move is accepted only when the transition probability is greater than a random number. The transition probability is a Boltzmann probability and is written as $e^{-\Delta E/k_B T}$, where $-\Delta E$ is the energy change, k_B is the Boltzmann constant and T is the temperature. After an initial equilibrium at fixed high temperature, the process continued as the temperature decreases (lower transition probability) and the energy should converge with an equilibrated coverage configuration. The total energy term (E_{total}) focuses on the binding energy of adsorbed molecules ($E_{binding}$) and Lennard-Jones interaction among the adsorbed molecules (E_{L-J}) as shown in Eq. 9.

$$E_{total} = E_{binding} + E_{L-J}$$
$$= \sum_{i=0}^{N} f_i \varepsilon_i + \frac{1}{2} \sum_{i=1}^{N} \sum_{j=1}^{N} f_i f_j \tilde{\varepsilon}(R_{ij}) \quad (9)$$

where

N : total number of adsorption sites (-)

f_x : occupation number as 1 or 0 at site, where $x \in \{i, j\}$ and $i \neq j$ (-)

ε_i : binding energy at site i (eV)

$\tilde{\varepsilon}(R_{ij})$: Lennard-Jones 12-6 potential at a distance of R_{ij}

, which is $4\lambda[(\frac{\sigma}{R_{ij}})^{12} - (\frac{\sigma}{R_{ij}})^{6}]$ where λ is the depth of the potential well and σ is the distance at which the potential is zero (eV)

The pseudo code is briefly described here. A 10 by 10 sites (N = 100) are used in this study. 1 sweep stands for proposing 100 steps and 1 step stands for flipping the occupation at the random chosen site. An acceptance ratio (AR) is used to monitor whether the parameters are suitable. AR should be over 80% during the initial equilibrium at fixed high temperature.

- Input: ε_i, σ, λ, N (= 100), CR (=0.999), T_0
- Step 0 (initial equilibrium at fixed high temperature, T_0):
  - For 10 sweeps:
    - For 100 steps:
      - Pick a random site: r_1 = rand[N]
      - Flip the occupation number: $f[r_1] = (1 + f[r_1])\ (1 - f[r_1])$
      - Calculate ΔE
      - Accept the move or not (rejection: flip it back)
        - If $\Delta E < 0$, accept the move. (continue)
        - If $\Delta E \geq 0$, then generate an acceptance number, r_2 = rand[0, 1). Accept the move if $e^{-\Delta E/k_B T} > r_2$.

- If $0 < AR < 0.8$, break and choose a new T_0

➢ SA with a series of decreasing temperatures: $T_n = CR \times T_{n-1}$

- While True:
  - Repeating the same procedure above for 100 steps
  - Break if 10 consecutive AR is zero (equilibrated)

➢ Output: equilibrated coverage (total sum of occupation number), final energy

The coding has passed some initial testing. For example, set σ equals the spacing between the sites nearby, we should expect 100% AR. Sensitivity check has also been gone through to check whether the code is robust for more sophisticated use. One of the results, initial AR (AR_i), steps to equilibrium (s_eq) and the saturated coverage, is shown in Fig. 3-1 with ε_i = -0.9 and σ = 0.25. The code is still in embryo and the future work is to use corresponding literature parameters for more sophisticated simulation. The combination with the existing DFT work is also expected.

- **Sigma = 0.25 :**

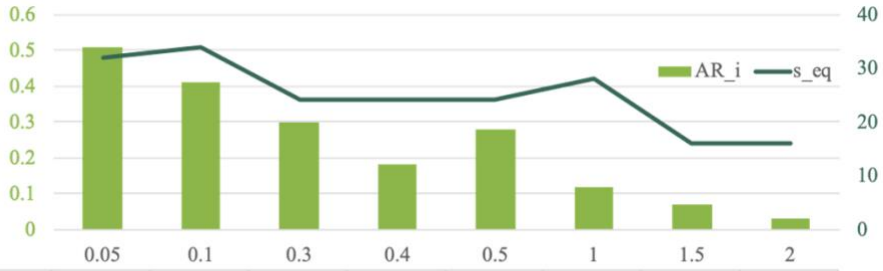

λ	0.05	0.1	0.3	0.4	0.5	1	1.5	2
AR_i	0.51	0.41	0.3	0.18	0.28	0.12	0.07	0.03
s_eq	32	34	24	24	24	28	16	16
coverage	0.43	0.43	0.42	0.48	0.48	0.50	0.45	0.43

Figure 3-1 Sensitivity check of initial AR, steps to equilibrium and coverage by varying λ when ε_i = -0.9 and σ = 0.25

3.2 Modification of LabVIEW setup for QCM-based reactor

The LabVIEW program for QCM system is modified (shown in Fig. 3-2) from the one by previous members. The added features are listed here:

1. MFCs control panel
2. Pressure and throttle valve openness recording
3. Multiple initial stages (typically for co-reactant pre-dose)
4. Sub-second exposure testing
5. Modified elapsed cycle timer

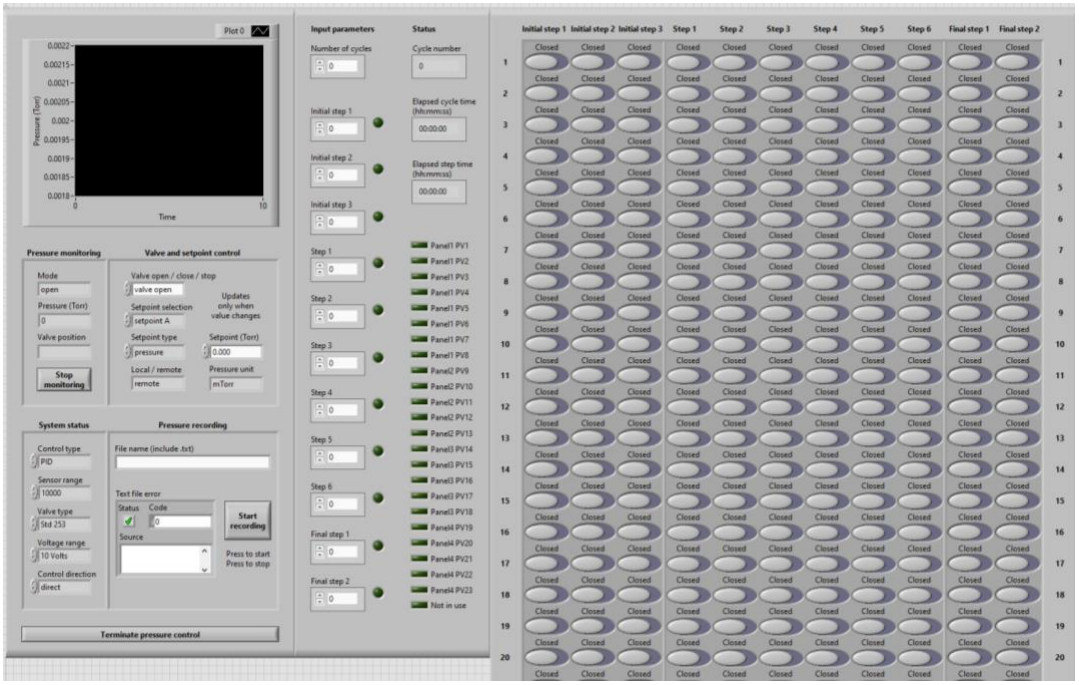

Figure 3-2 Screenshot of the six-step LabVIEW program for QCM system

4. Experimental approach

4.1 Sample preparation

4.1.1 Coupon samples

The samples used in this study come as 300 mm wafers. Three types of substrates are Co (15 nm Co|100 nm SiO_2|Si), Cu (100 nm PVD Cu|Ta (adhesion layer)|SiO_2 wafers) and native oxide on Si (100) wafer (Boron doped, resistivity 38 – 63 Ω-cm). For most cases, the substrates are cleaved (i.e., scribed and diced) and used as-received. For more quantitative work, chemical oxide on silica is prepared from cycles of buffer oxide etch (BOE)/Nanostrip treatment and it is known to produce a 15-20 Å layer with surface hydroxyl group Si-OH density of ~ 5×10^{14} cm^{-2} [36,42]. The treatment consists of 2 minutes dipping in BOE to etch off the native oxide and 15 minutes of dipping in Nanostrip at 75°C to form surface hydroxyl groups. The samples are used within a week to ensure the quality.

To conduct experiments on clean and reproduceable samples, surface cleaning techniques have been studied as well. The most typical one is annealing. As mentioned in Ch. 2.2, the sample heater equipped with the sample manipulator could heat the samples directly and could be controlled based on the calibrated values. The post-annealing samples are analyzed with XPS and the oxide peaks are specifically inspected for metal substrates. On Cu samples, the oxide (CuO) satellite peak of Cu 2p 3/2 is roughly around 943 eV and the Cu LMM Auger peak will shift toward lower BE if copper oxide is present [23]. Cleaning Cu samples with ozone plasma has also been studied before by previous members. For chemical oxide or native oxide,

it is reported that the surface hydroxyl groups are sufficient when the samples are heated below 200°C [44,45].

Various approaches to produce a clean Co surface are reported in the literature and most of them focused on cycles of annealing and ion sputtering [16,46–48]. Annealing expedites the process of carbon segregation at the surface and sputtering could remove the surface carbides and oxides. The annealing temperature is important to be controlled below 700K since it is the temperature at which phase transition from hcp cobalt to fcc cobalt takes place. An amorphous cobalt would be hard for simulation and thus maintaining a fcc-structure cobalt substrate is better for the combination of experimental and computational work. In our study, we have tried annealing at 330°C under UHV and various duration of Ar^+ sputtering at 1 keV and the results are shown in Fig. 4-1. The annealing temperature at 270°C was later proved to be effective as well. The sputtering step in our case seemed to have no significant impact compared to annealing regarding having a less-oxide surface. It is suspected that since there is only 15 nm of Co on the samples, annealing might be sufficient for oxygen and carbon diffusing to surface and they escape as gas species. Sputtering could be destructive to a thin film.

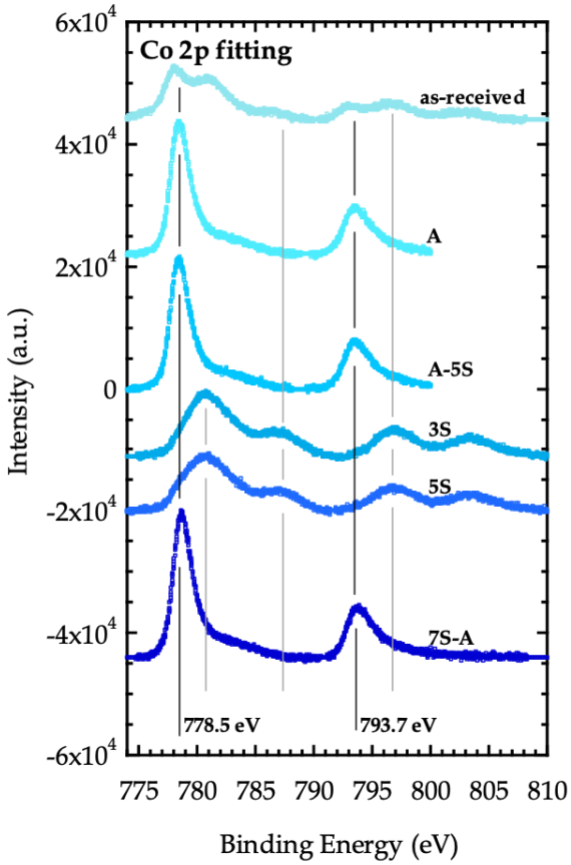

Figure 4-1 Summary of XP spectra for Co(2p) from as-received and post-treatment cobalt coupons (A: annealing at 330°C / xS: Ar^+ sputtering at 1keV for x seconds / "-": treatment in sequence)

4.1.2 QCM quartz crystals

QCM gold electrode crystals (INFICON, 750-1058-G10) are purchased as 120°C crystals (operation temperature from 112 °C to 128 °C). To make the starting surface as silica (direct study), the gold crystals are deposited with SiO_2 ALD at CCMR. Customized copper electrode

crystals from INFICON are purchased as received. A single crystal is then loaded onto the housing. QCM could only study one type of substrate at a time. There is a platform that has also been mounted onto the ALD sensor so that the coupon samples could be placed on there and be analyzed with XPS later. The samples will inevitably experience an air break before analyzed by XPS in the micro-reactor/UHV system.

4.2 Micro-reactor setup

First, the micro-reactor setup is discussed here. After loading and transferring the sample holder to the sample manipulator, the annealing process is started under UHV. The heater power is adjusted based on the setpoint and the calibration. Once the reference temperature has reached the calibrated value, the process lasts for 30 minutes. During the process, the reference temperature is monitored and heating rate is adjusted to stay at the calibrated temperature. Subtle changes during loading every time, such as the tightness of the screws on the sample holder and the tightness of the sample holder onto the sample manipulator, would lead to variation in heating efficiency and thus reference temperature. After annealing, main gate valve is closed and intermediate chamber is pressurized by starting curtain flow. The heating power is then adjusted to the calibrated value based on the reaction temperature under higher pressure. Reactor gate valve could then be opened and the micro-reactor lines are ready to be moved in by translational stage. PID pressure control (a system of Baratron, pressure controller and throttle valve) is initiated with a given setpoint.

As mentioned before, the velocity and position translational stage could be controlled. Initially, it moves in at a higher velocity and then it approaches at a lower rate and smaller step

size when it is near the sample holder. With a multimeter to test the resistance among the four probes (testing two probes at a time), the reactor lines stops at the position where three or four probes are showing single-digit resistance and the sample holder could be visually seen to be slightly pushed back. Heating elements for delivery lines and reactor lines are turned on for at least 20 minutes prior to the experiments. The three reactor lines are heated to around 100°C and the two effluent lines are heated to around 60°C with the tungsten heating elements. The delivery lines are heated based on the delivered chemicals and the purpose is to prevent they from condensing on the wall. For example, the lines for 4-octyne and H_2O are at room temperature since the vapor is at low temperature (bubblers are placed in ice baths to suppress the partial pressure). However, TEMAZ/TEMAHf line is always heated to 70°C (bubbler is in a 40°C water bath) since we once found a clogging at the downstream elbow without heating the line then. The flows are controlled at the given mass flow rates and as purge status (all purge flows are directed to the reactor while all carrier flows toward E2M8) for stabilization before the experiment. LabVIEW program is set up by entering the MFC conditions, configuration of the pneumatic valves and the duration of each step. The experiment starts once the program runs. The carrier flow could be controlled by the bypass manual valve as flow through bubbler (close bypass) or flow over vapor (open bypass). To minimize the lingering of the chemicals in the waste lines, the manual valves at the inlet and outlet of the bubblers are opened 1 minute before the exposure instead of being opened all the way through. There is a specific sequence for turning the three manual valves to minimize a gas accumulation (open outlet, open inlet and then close bypass for flowing through bubbler; inverse the sequence and valve status for closing the bubbler). The reactor lines are retracted and all flows and heating elements are turned off after the experiment.

4.3 QCM reactor setup

For the QCM system, details would be described elsewhere. The furnace is first set to desired anneal setpoint. After the crystal and coupon samples are loaded, the QCM sensor feedthrough is guided into the reactor tube which is wrapped around by a furnace (a hot-wall reactor). The annealing proceeds for at least one hour. The experiments are carried out with LabVIEW program and the pneumatic valves system as well in a similar manner as with micro-reactor system (mentioned in Ch. 4.2). A cycle feature depends on the microscopic reaction mechanism and thus it is especially important to observe the apparent mass change during the exposures of reactants, i.e., precursor and co-reactant.

The carrier flow used in this system is argon. An specific flow that is rather essential in QCM system is the backside purge line (labeled as the flow on panel 1-1), which is a flow through the backside of the QCM crystal and is deigned to flow against those carrying reactants to prevent the sensitive crystal from any deposition on the backside. Carrier flows from panel 2, 3 and 4 are for precursor (TEMAZ), co-reactant (H_2O) and co-adsorbate (4-octyne) respectively. The pressure in the reactor tube is also PID-controlled at the desired setpoint. The crystal surface temperature has been calibrated by soldering a thermocouple on the crystal and the furnace controller. The purge and carrier flow lines are not separated in QCM system thus the flow on the panel is either purging or flowing through the bubbler, which is controlled by the pneumatic valves. Delivery lines on the three panels are wrapped with heating element. During an experiment, the delivery line on panel 2 and 4 are always heated to 80 °C and that on panel 3 are heated to 100 °C. Water and ice baths are used as well for the corresponding bubblers.

4.4 Process design

Both Micro-reactor/UHV and QCM systems are equipped with pneumatic valves that could be controlled automatically by LabVIEW program. Based on this, various process sequence could be achieved for different purposes. In this section, the process design focuses on the process of thin film deposition with or without the introduction of co-adsorbate.

4.4.1 Experimental conditions

Several experimental conditions are mainly investigated in this study. Substrate temperature is critical for the reactivity at the surfaces in a thermal CVD/ALD process, especially given that the micro-reactor is sort of a cold-wall reactor. In the meanwhile, it affects the chemisorption of the co-adsorbate significantly as well. The substrate temperature window is 120°C, 150°C, 180°C or 240°C. As discussed in Ch. 2.2.3, pressure has large impact on the flow dynamics and 1.5 Torr, 9 Torr or 18 Torr is studied. Flow rates influence the concentration (partial pressure) of the delivered chemicals in the reaction zone. Besides, the flow ratio of all flows from the panels (flow A, B and C) to curtain flow and the total flow rate are parameters as well. In some cases, both carrier (carrying chemical) and purge flows are both introduced into the reactor for dilution (e.g., 1 sccm N_2 carrier flow through H_2O bubbler + 4 sccm N_2 purge flow, compared to 5 sccm N_2 carrier flow through H_2O bubbler). The duration of each exposure step is the essential topic in thin film deposition. Since our study focuses on the introduction of the co-adsorbate, gas-phase interactions are more complicated and different process designs are required to be studied. Illustrations for different exposure sequences are shown in the following sections. The durations are more qualitative and arbitrary for the big picture.

4.4.2 Pristine CVD and ALD

The schematics for pristine CVD and ALD are shown as (a-1) and (b-1) respectively in Fig. 4-2. These rudimental experiments are important whenever there is a new experimental setup and will be the baseline to be compared with any further study. For pristine CVD results, a basic relation between the film thickness (calculated from XPS results) and the duration of co-reactant exposure should be linear. For pristine ALD results, growth per cycle (GPC) is the constant slope observed in the film thickness versus cycle numbers.

4.4.3 CVD with co-adsorbate

The schematic for CVD with co-adsorbate is shown as (a-2) in Fig. 4-2. This would be a more complicated case since the gas-phase chemical interactions are among the three species. The flow dynamic plays a vital part in this as well since a perfect mixing should be achieved in the reaction zone.

4.4.4 A-B-C cycle ALD

An A-B-C cycle ALD is important in this study since it will test out the reversible chemisorption of the co-adsorbate. Thus, the result from A-B-C cycle ALD should be observed to be similar as that from a pristine ALD. The blocking layer on the surface theoretically should be removed (physical bombardment by the purging species) during the purge step before every dose of precursor.

4.4.5 ALD with co-adsorbate

There are two ways to introduce the co-adsorbate in an ALD experiment. The schematic for ALD with co-adsorbate during precursor is shown as (b-3) in Fig. 4-2. This exposure sequence is the main setup in this study since the gas-phase interaction is simplified as only between precursor and co-adsorbate. Generally speaking, the reactivity between these two (amine and alkyne) should be low. Another case could be studied is ALD with co-adsorbate continuous, which is shown as (b-4) in Fig. 4-2. Again, the interaction involves co-reactant and based on some results, this might be problematic since the co-adsorbate might react and already loose its functionality in gas phase. However, this still could be studied further in the future.

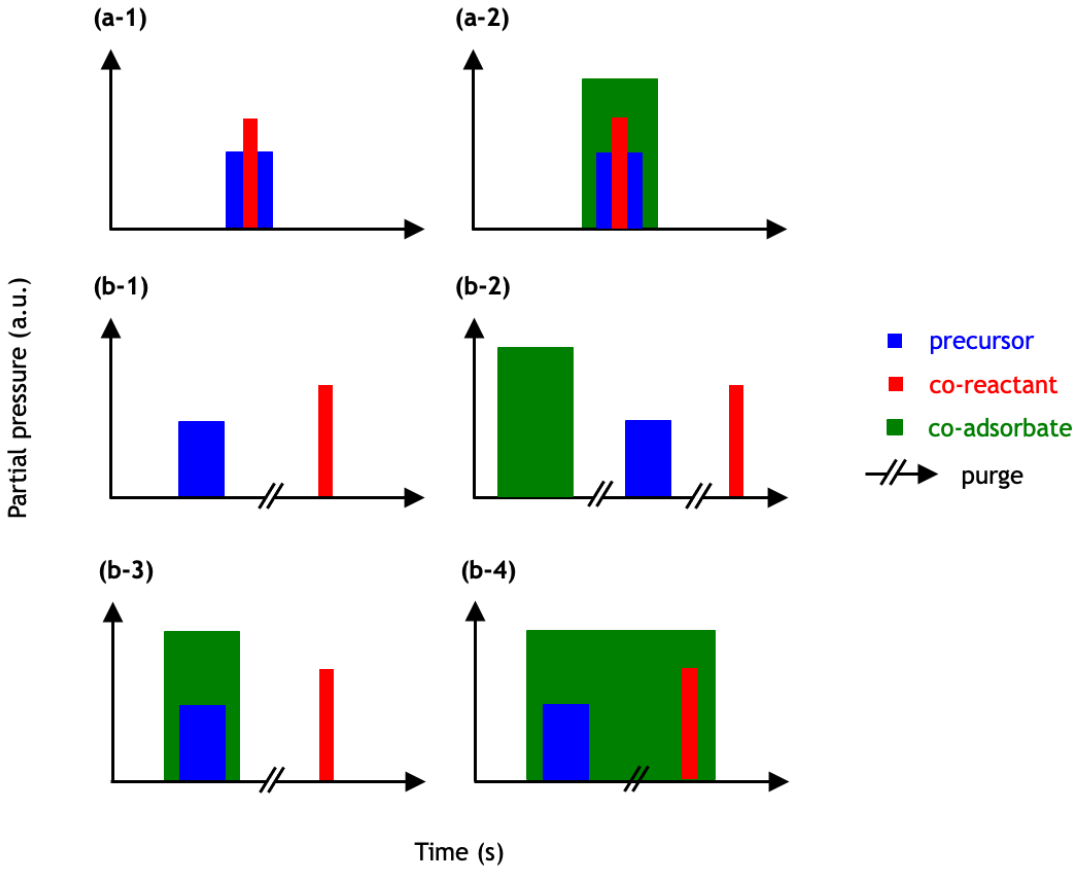

Figure 4-2 Summary of schematics for exposure sequence: (a-1) pristine CVD; (a-2) CVD with co-adsorbate; (b-1) pristine ALD; (b-2) A-B-C cycle ALD; (b-3) ALD with co-adsorbate during precursor; (b-4) ALD with co-adsorbate continuous. The length of exposure is arbitrary. The initial and final states are always at purge state. The exposure sequence of ALD shown here is as per cycle

5. Results and discussions

5.1 4-octyne partial pressure measurement

As mentioned in Ch. 1.4, the partial pressure of the co-adsorbate, 4-octyne, is critical to the competitive adsorption. To mimic the real experimental conditions, procedure is similar to that mentioned in Ch. 4.2, except the pressure controlling step to be started with. The 4-octyne bubbler was placed in the ice bath. After all the three purge flows are introduced into micro-reactor (purge state) and the pressure is under PID control at the setpoint, the openness of the throttle valve is recorded. Then, PID control is turned off and the throttle valve is controlled to be fixed at this value. Now, the pressure should be stable around the setpoint at purge state. The following operation is conducted with the manual LabVIEW program. For the 4-octyne partial pressure measurement, the purge flow rate and carrier flow rate on panel A (for co-adsorbate) vary based on different dilution rate. The carrier flow is directed through the bubbler and to E2M8 for the initial stabilization. Once the fore-line pressure is stable, pneumatic valves are set up to introduce the flow(s) into micro-reactor. A rise in Baratron pressure should be observed and the stabilized pressure is recorded after a few minutes. 4-octyne partial pressure is calculated as the pressure difference (= $P_{stabilized} - P_{setpoint}$). The results are shown in Fig. 5-1. The linear fitting lines for the three cases roughly went through the origin.

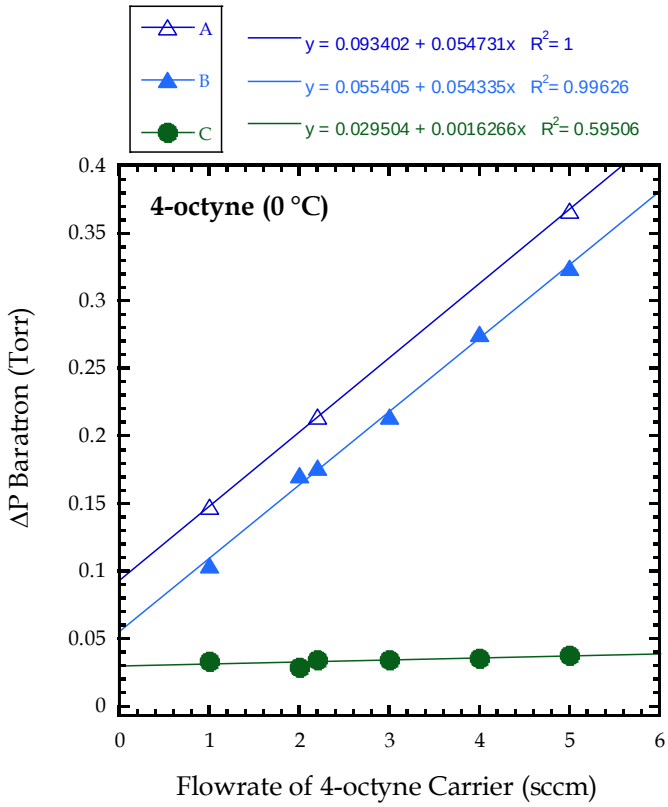

Figure 5-1 4-octyne partial pressure (ΔP Baratron) versus the carrier flow rate for 4-octyne. **Case A**: 10 sccm as curtain flow and 5 sccm in total on 4-octyne panel (15 sccm in total). **Case B**: 6 sccm as curtain flow, 2 sccm each on other two panels and 5 sccm in total on 4-octyne panel (15 sccm in total). **Case C**: 6 sccm as curtain flow, 5 sccm each on other two panels and 5 sccm in total on 4-octyne panel (25 sccm in total)

5.2 4-octyne chemisorption on copper and silica

With QCM, the real-time chemisorption of 4-octyne on copper and silica (Au-SiO_2) crystals could be captured. The mass uptake should theoretically be saturated when the saturation coverage has been reached since the adsorption sites are limited. Besides, once the 4-

octyne exposure has stopped and the surface is purged, the mass uptake should decrease based on the expectation of reversible adsorption.

In Fig. 5-2, the QCM results for four 50s of 4-octyne pulses followed by different length of purging on a 120°C Cu crystal are shown. It is evident that the adsorption of 4-octyne was reversible and with a sufficient purging, full desorption could be expected in Fig. 5-2 (a). More straightforwardly in Fig. 5-2 (b), the steady-state coverages of 4-octyne were roughly saturated after 10s and it remained till the pulses were stopped. The pulse shapes were very consistent as well. Moreover, the mass uptake and desorption sections were fitted well with the first-order Langmiur model, which indicated over 80% of surface coverages. As a whole, this result has perfectly supported the expectation for 4-octyne adsorption on copper.

Another sets of experiments have been done on the two types of crystals. The experimental conditions are shown in Table 5-1. Under the same conditions, the QCM results of 10 cycles 4-octyne exposure on copper and silica surface are shown in Fig. 5-3. The 4-octyne adsorption on silica surface might lead to the formation of a carbonaceous film and thus the cycle feature was not significant, which could support that adsorption of 4-octyne on silica surface is not favorable. As for the behavior on the copper surface, there was a mass uptake at the first cycle and the apparent mass had the tendency to decrease. There is a possible explanation with the temperature effect on the QCM crystal. First, the 4-octyne partial pressure was roughly at 0 °C (bubbler was placed in the ice bath). Secondly, unlike on silica surface, there was frequent adsorption and desorption of 4-octyne on the surface (theoretically speaking), which could accelerate the temperature loss process. Consequently, the temperature would drop more significant on copper surface due to the continuous exposure of the low-temperature 4-

octyne flow. As the heated flows continued to flow over the cooled-down crystal, there would be a negative apparent mass change (mentioned in Ch. 1.7).

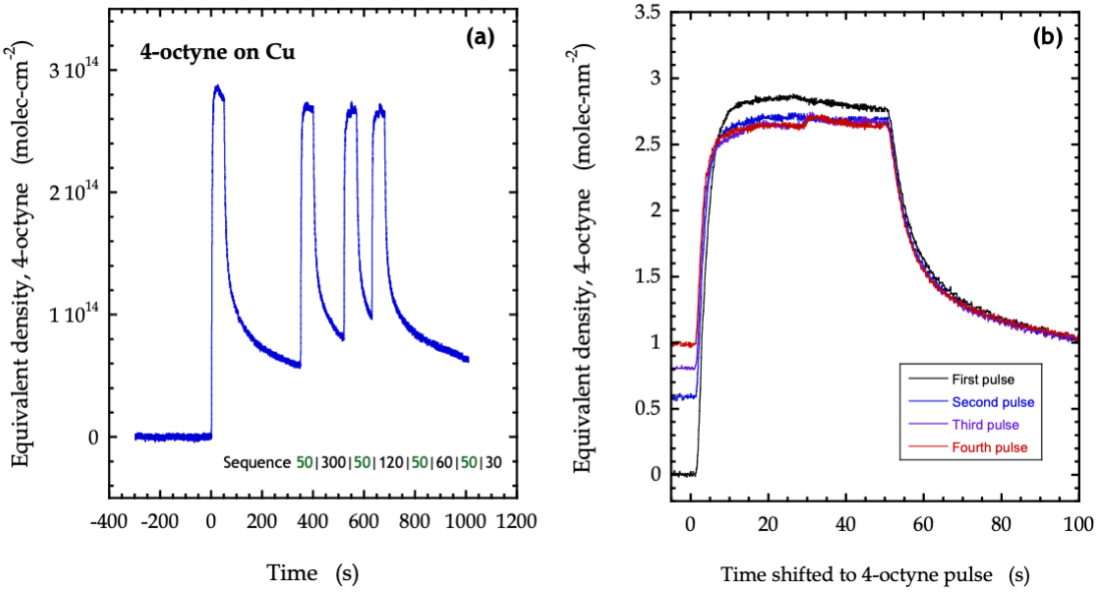

Figure 5-2 (a) The equivalent density of 4-octyne versus the exposure time from four 50s of 4-octyne pulses followed by 300s, 120s, 60s and 30s of purging on a 120°C Cu crystal (b) Four 50s 4-octyne pulses shifted to the same starting point

4-octyne Exposure on Au-SiO_2 and Cu crystals		Panel	Carrier Flowrate (sccm)
		1-1	10
P (Torr)	1.5	2	21
Ts (°C)	120	3	21
Cycles	10	4	3
Exposure Sequence			
step	species	duration (s)	state
1	4-octyne	50	co-adsorbate
2		70	purge

Table 5-1 Experimental conditions for 4-octyne exposure with QCM system

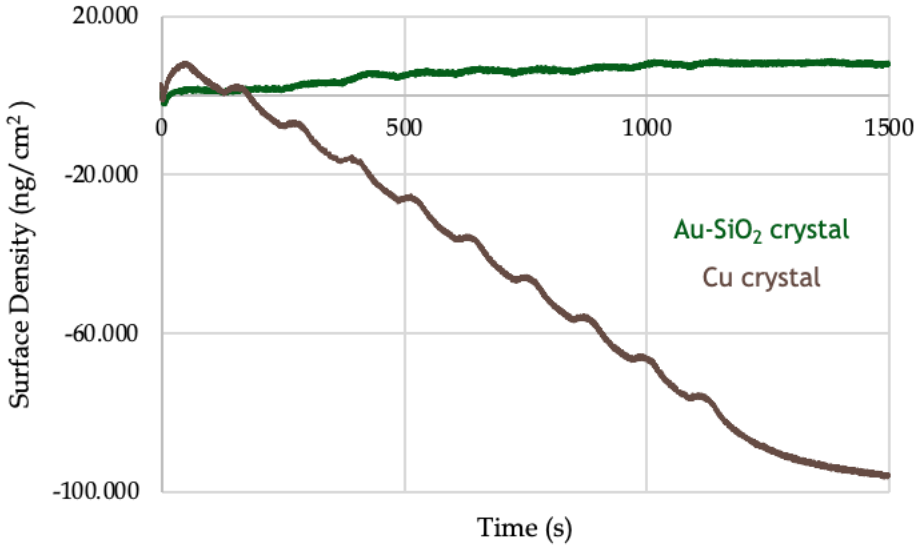

Figure 5-3 QCM results of 4-octyne exposure on Cu and Au-SiO_2 crystals under the conditions shown in Table 5-1

5.3 Pristine CVD and ALD study

Due to various objectives throughout the research, multiple sets of experimental conditions have been tested and some representative results are discussed here. The process sequence is shown as Fig. 4-2 (a-1) and (b-1). The thickness calculation from XPS results herein is mentioned in Ch. 2.2.4.2 (calculated directly from the models with reference intensities).

5.3.1 Zirconia deposition

Since the metal amine precursor tends to have a lower partial pressure under ambient condition (below 0.01 Torr, shown in Fig. 2-1), the TEMAZ bubbler is always placed in a hot

water bath, which is at 50°C in the QCM system while it is at 40 °C in the micro-reactor system. The GPC values of zirconia by thermal ALD with TEMAZ and $H_2O_{(g)}$ from previous work are reported as approximately 0.80-0.97 Å-cycle^{-1} [36,49,50]. The value of thermal ALD with O_2 is reported as below 0.5 Å-cycle^{-1}, which is reasonable since O_2 is a weaker oxidant than H_2O [50].

The experimental conditions for ZrO_2 ALD with QCM system are shown in Table 5-2 and the results are shown in Fig. 5-4. The assumption of a constant GPC is viable here due to the linearity between the thickness and time. The calculated GPCs are 0.83 Å-cycle^{-1} with Cu crystal and 0.85 Å-cycle^{-1} with Au-SiO_2 crystal respectively, which are comparable with the reported values.

Pristine ZrO_2 ALD on Au-SiO_2 and Cu crystals		**Panel**	**Carrier Flowrate (sccm)**
		1-1	10
P (Torr)	1.5	2	21
T_s (°C)	120	3	21
Cycles	30	4	3
Exposure Sequence			
step	**species**	**duration (s)**	**state**
1	H_2O	10	co-reactant predose
2		50	purge
3-1	TEMAZ	30	precursor
3-2		15	purge
3-3	H_2O	3	co-reactant
3-4		72	purge

Table 5-2 Experimental conditions for ZrO_2 pristine ALD with QCM system

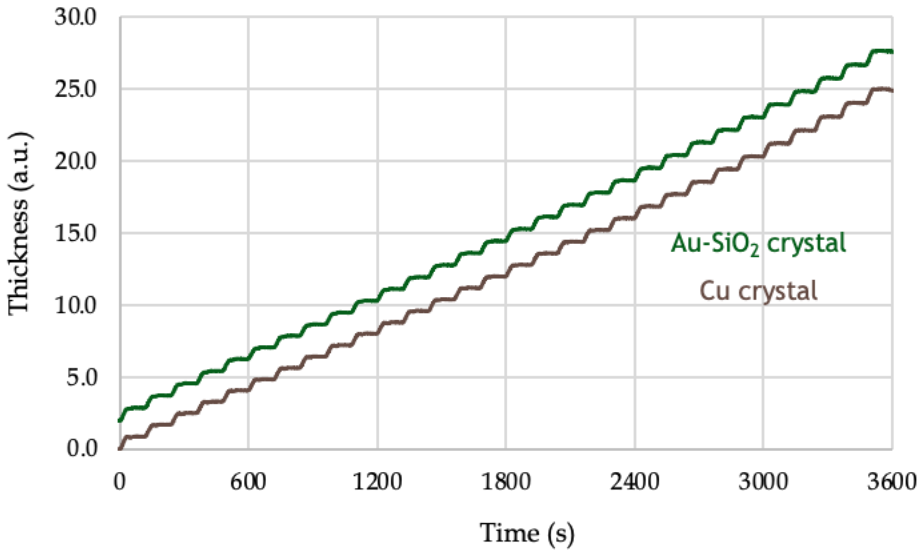

Figure 5-4 QCM results of ZrO_2 pristine ALD on Cu and Au-SiO_2 crystals under the conditions shown in Table 5-2

The experimental conditions for ZrO_2 CVD on native oxide with micro-reactor system are shown in Table 5-3 and the results are shown in Fig. 5-5. Under the assumption of that the deposited films were ZrO_2 and homogeneous, the thicknesses on both silica surfaces are calculated in Table 5-4 from the buried substrate model.

Pristine ZrO_2 CVD on 2 native oxide coupons		Panel	Carrier Flowrate (sccm)
		curtain	6
P (Torr)	1.5	A	3
T_s (°C)	120	B	2 (purge) + 1 (carrier)
		C	3
Exposure Sequence			
step	**species**	**duration (s)**	**state**
1	TEMAZ	120	precursor
2	TEMAZ | O_2	2	precursor & co-reactant
3	TEMAZ	25	precursor

Table 5-3 Experimental conditions for ZrO_2 pristine CVD with micro-reactor system (15 sccm total flow, on two silica samples)

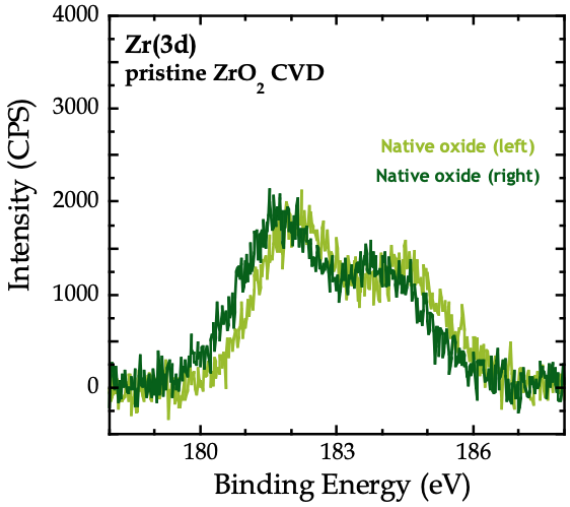

Figure 5-5 Zr(3d) XP spectra for ZrO_2 pristine CVD on two silica substrates under the conditions shown in Table 5-3

	Sample	Intensity (raw area) [CPS-eV]					Sum [CPS-eV]	Peak BE [eV]	Peak KE [eV]	mfp[Å] in ZrO_2 with Mg(1249.1 eV)	ZrO_2 thickness [Å]
Pristine ZrO_2 CVD	Native oxide (left)	Si2p3/2	SiO2	Si2O3	SiO	Si2O		Si(2p3/2)			5.83
		5926.73	1693.78	0.001	0.001	0.001	7620.51	98.05	1151.05	20.75	
	Native oxide (right)	Si2p3/2	SiO2	Si2O3	SiO	Si2O		Si(2p3/2)			4.40
		6172.08	1885.37	0.001	0.001	264.487	8321.94	97.6	1151.50	20.76	
180°C annealed Chemox	Chemox	Si2p3/2	SiO2	Si2O3	SiO	Si2O		Si(2p) unattenuated base (substrate)			
		9392.15	1518.37	0.001	0.001	0.001	10910.52				

Table 5-4 Thickness calculation for ZrO_2 pristine CVD on two silica substrates under the conditions shown in Table 5-3

The experimental conditions for ZrO_2 CVD on copper and cobalt with micro-reactor system are shown in Table 5-5 and the results are shown in Fig. 5-6. Under the assumption of that the deposited films were ZrO_2 and homogeneous, the thicknesses on Co and Cu surfaces are calculated in Table 5-6 from the buried substrate model.

Pristine ZrO_2 CVD on Cu and Co		**Panel**	**Carrier Flowrate (sccm)**
		curtain	10
P (Torr)	1.5	A	5
T_s (°C)	120	B	4 (purge) + 1 (carrier)
		C	5
Exposure Sequence			
step	**species**	**duration (s)**	**state**
1	TEMAZ	120	precursor
2	TEMAZ | O_2	2	precursor & co-reactant
3	TEMAZ	25	precursor

Table 5-5 Experimental conditions for ZrO_2 pristine CVD with micro-reactor system (25 sccm total flow, on Co and Cu samples)

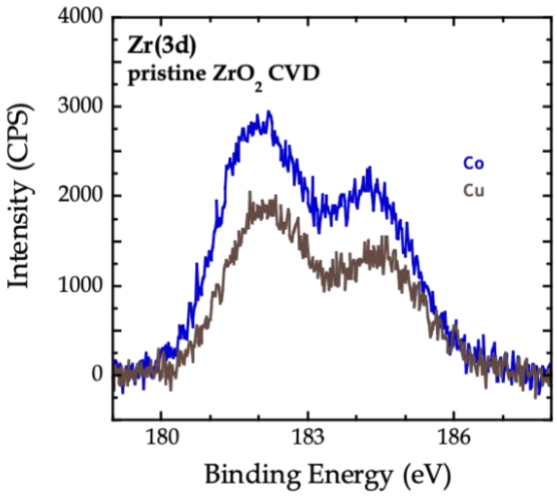

Figure 5-6 Zr(3d) XP spectra for ZrO_2 pristine CVD on Co and Cu substrates under the conditions shown in Table 5-5

	Sample	Intensity (raw area) [CPS-eV]						Sum [CPS-eV]	Peak BE [eV]	Peak KE [eV]	mfp[Å] in ZrO_2 with Mg(1249.1 eV)	ZrO_2 thickness [Å]
Pristine ZrO_2 CVD	Cu	Cu metal	oxidized Cu (1)	oxidized Cu (2)					Cu(2p3/2)			8.69
		1772.32	34266.3	3171.77				39210.39	931.27	317.83	8.39	
	Co	Co(3/2)	Co oxide (3/2)						Co(2p3/2)			8.66
		16172	1088.88					17260.88	778.51	470.59	10.83	
180°C anneal Cu	Cu	Cu metal	oxidized Cu (1)	oxidized Cu (2)					Cu(2p) unattenuated base (substrate)			
		130574	6595.95	10190.8				147360.75				
180°C annealed Co	Co	Co(3/2)	Co oxide (3/2)						Co(2p) unattenuated base (substrate)			
		15274.1	32665.5					47939.60				

Table 5-6 Thickness calculation for ZrO_2 pristine CVD on Co and Cu substrates under the conditions shown in Table 5-5

5.3.2 Hafnia deposition

The TEMAHf bubbler was placed in a water bath at 40 °C in the micro-reactor system. The GPC values of hafnia by thermal ALD with TEMAHf and H_2O from previous work are

reported as approximately 0.66-0.72 Å-cycle^{-1} [51,52] or 1.10-1.25 Å-cycle^{-1} [14,50]. The value of thermal ALD with O_2 is reported as below 0.2 Å-cycle^{-1} [50].

The experimental conditions for HfO_2 CVD with 1s, 5s and 10s exposure of O_2 (co-reactant) with micro-reactor system are shown in Table 5-7. Theoretically for a CVD experiment, the thin film growth (indicated by the intensity area of Hf(4f)) should be linear with the exposure length of co-reactant. However, the linearity was not observed in Fig. 5-7 and the growth seemed to be saturated. Some suspicions included the low partial pressure of the precursor (TEMAHf), low reactivity of co-reactant (O_2) or poor confinement that led to a prolonged CVD experiment that was irrelevant to the exposure durations.

Pristine HfO_2 CVD on Cu and native oxide coupons		**Panel**	**Carrier Flowrate (sccm)**
		curtain	6
P (Torr)	1.5	A	3
T_s (°C)	120	B	3
		C	3
Exposure Sequence			
step	**species**	**duration (s)**	**state**
1	TEMAHf	120	precursor
2	TEMAHf | O_2	1/5/10	precursor & co-reactant
3	TEMAHf	25	precursor

Table 5-7 Experimental conditions for HfO_2 pristine CVD with micro-reactor system

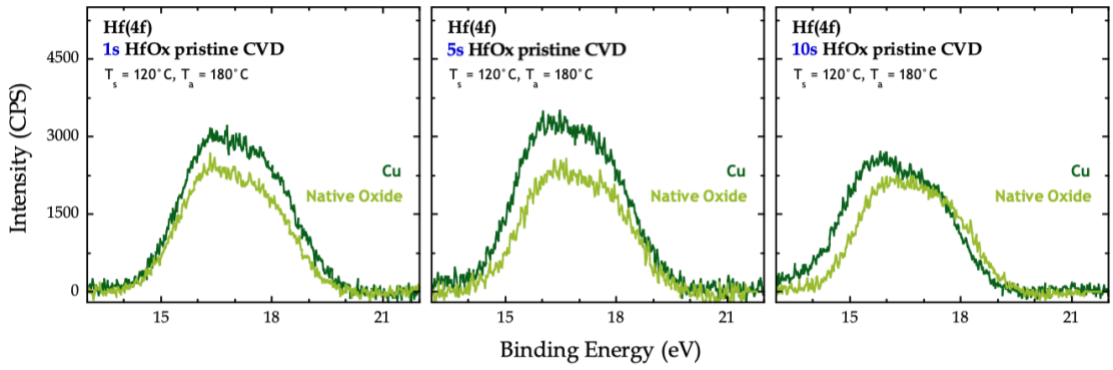

Figure 5-7 Hf(4f) XP spectra for HfO_2 pristine CVD on silica and Cu substrates under the conditions shown in Table 5-7

The experimental conditions for HfO_2 ALD with micro-reactor system are shown in Table 5-8. The Hf(4f) XP spectra for ALD with O_2 are shown in Fig. 5-8 (a) to (c) and ALD with H_2O are shown as (d) to (f) . Under the assumption of that the deposited films were HfO_2 and homogeneous, the calculated thicknesses versus ALD cycle numbers are shown in Fig. 5-9 from the buried substrate model. For those from ALD with O_2, the linearity was fitted better with the thin film model. Under the assumption of that the deposited films were HfO_2 with either H_2O or O_2, the reference intensity (a semi-infinite film) was from the 10 cycles of HfO_2 ALD with H_2O, which is shown as (f) in Fig. 5-8. The explanation could be that the inelastic scattering which the electrons from Si atom had gone through was significant due to the inhomogeneous (not as perfect crystal) deposited films. From the comparison between the results with H_2O and those with O_2, the GPC with H_2O was much higher (4.73 Å-cycle^{-1} on Cu and 6.58 Å-cycle^{-1} on native oxide), which was reasonable since water is a stronger oxidant but differed from the value for a typical ALD process. It could be due to, again, the poor confinement of the reaction zone or unknown side reactions had occurred by using water as co-reactant. On the other hand,

the GPC from ALD with O_2 calculated from the thin film model (1.08 Å-cycle^{-1}) matched well with the literature values.

Pristine HfO_2 ALD		Panel	Carrier Flowrate (sccm)
		curtain	49
P (Torr)	9	A	7
T_s (°C)	180	B	3.5
Cycles	1/5/10	C	7
Exposure Sequence			
step	**species**	**duration (s)**	**state**
1-1	TEMAHf	120	precursor
1-2		120	purge
1-3	H_2O / O_2	30	co-reactant
1-4		120	purge

Table 5-8 Experimental conditions for HfO_2 pristine ALD with micro-reactor system

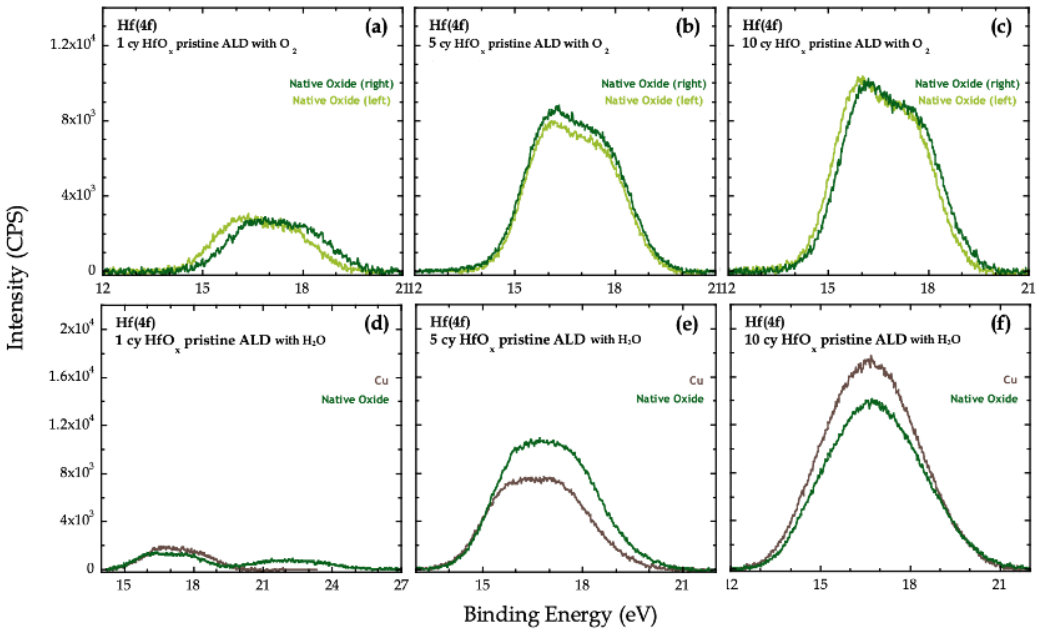

Figure 5-8 Hf(4f) XP spectra for 1, 5 and 10 cycles of HfO_2 pristine ALD with O_2 on two silica substrates under the conditions shown in Table 5-8 are shown respectively as (a), (b) and (c). Those with H_2O on Cu and silica substrates are shown respectively as (d), (e) and (f)

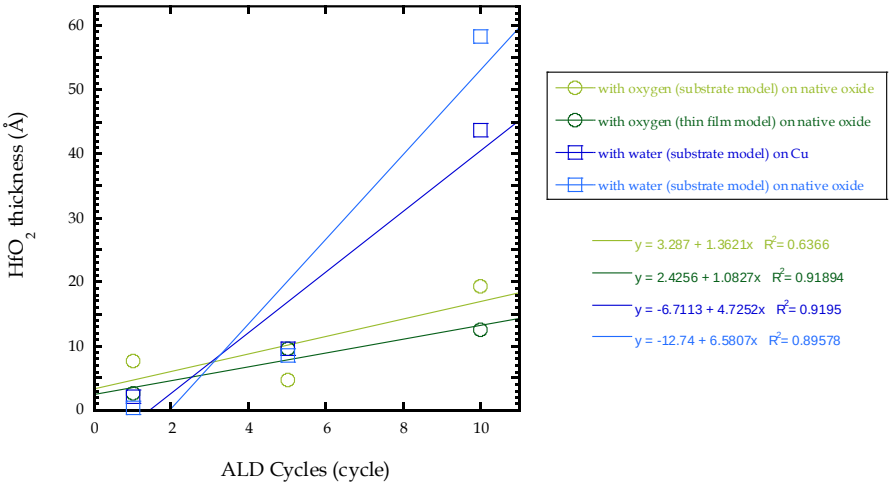

Figure 5-9 HfO_2 thickness versus pristine ALD cycle numbers. GPCs are presented as the slopes.(only the results on the right silica substrate for ALD with oxygen are shown here)

5.4 Co-exposure study: 4-octyne and TEMAHf

The gas phase interactions are rather vital and influential to the following surface reaction. Thus, since some of the results are not as expected, an experiment of TEMAHf and 4-octyne co-exposure was conducted to observe whether 4-octyne was able to block the metallic surface or else participate in the deposition. Ideally, the results should be traces of hafnium signals on copper since a portion of reaction sites would be occupied by 4-octyne.

The experiment was conducted with both substrates annealed at 180°C, the bath temperature for 4-octyne at 13°C and other experimental conditions are shown in Table. 5-9. The less-ice bath was prepared with a fix amount of ice and a thermometer kept for monitoring the temperature. The purpose was to augment the partial pressure of 4-octyne to amplify the interaction. The results are shown in Fig. 5-10 and they were showing the expectations. Consequently, there is still other issues that were affecting the experiments.

Co-exposure of 4-octyne & TEMAHf on Cu and native oxide coupons		**Panel**	**Carrier Flowrate (sccm)**
		curtain	6
P (Torr)	1.5	A	3
T_s (°C)	120	B	3
		C	3
Exposure Sequence			
step	**species**	**duration (s)**	**state**
1	4-octyne	30	co-adsorbate
2	TEMAHf | 4-octyne	150	precursor & co-adsorbate
3	4-octyne	30	co-adsorbate

Table 5-9 Experimental conditions for TEMAHf and 4-octyne co-exposure with micro-reactor system

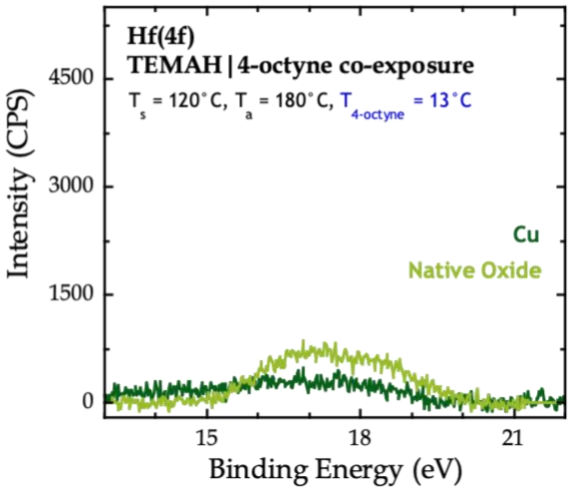

Figure 5-10 Hf(4f) XP spectra for TEMAHf and 4-octyne co-exposure on silica and Cu substrates under the conditions shown in Table 5-9

5.5 ALD and CVD with co-adsorbate

The representative results of area-selective deposition by introducing co-adsorbate are shown here. Successful results of selective deposition of zirconia on chemical oxide exclusively instead of copper surface are published [23,42]. The results herein are the follow-up studies including using another precursor (TEMAH), different co-reactant (O_2, H_2O or wet O_2), cobalt substrate and QCM studies.

5.5.1 ALD with co-adsorbate during precursor

With the proposed mechanism shown in Fig. 1-2, the QCM results for two ALD cycles with TEMAZ and water are shown to capture the minute mass change on the surface in Fig. 5-11 [4]. Similar trend could also be observed with our QCM system on both Au-SiO_2 and Cu

crystals. The zoom-in results from one of our experiments at the 15th cycle are shown in Fig. 5-12. The experiments here were 30 cycles ALD with TEMAZ, water and 4-octyne as the co-adsorbate. The exposure sequence were shown in Table 5-10 with steps from 1 to 3-6; thus, TEMAZ exposure was from 15s to 45s and water exposure was from 60s to 63s (small time delay was accumulated from QCM sampling, LabVIEW timer and communication). The typical mass uptake was observed during the former on the surface while the apparent mass decrease during the latter occurred due to the substitution of dialkylamine ligands with hydroxyl groups. Some temperature effect might have played some part in this. The suppression of growth on Cu surface could also be observed. The cycle feature, the shape, matched with the proposed one.

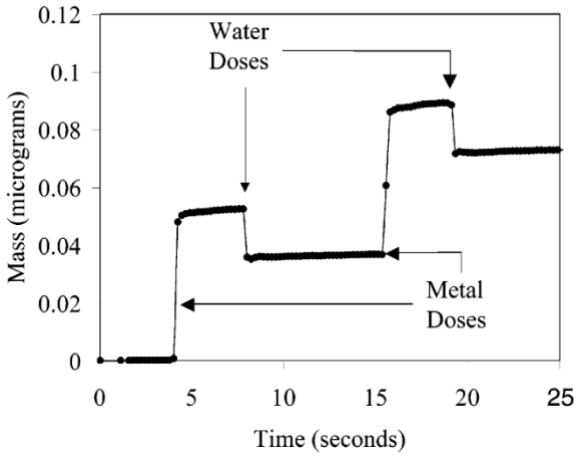

Figure 5-11 QCM mass changes during two ALD cycles with TDMAZ and water at 200°C

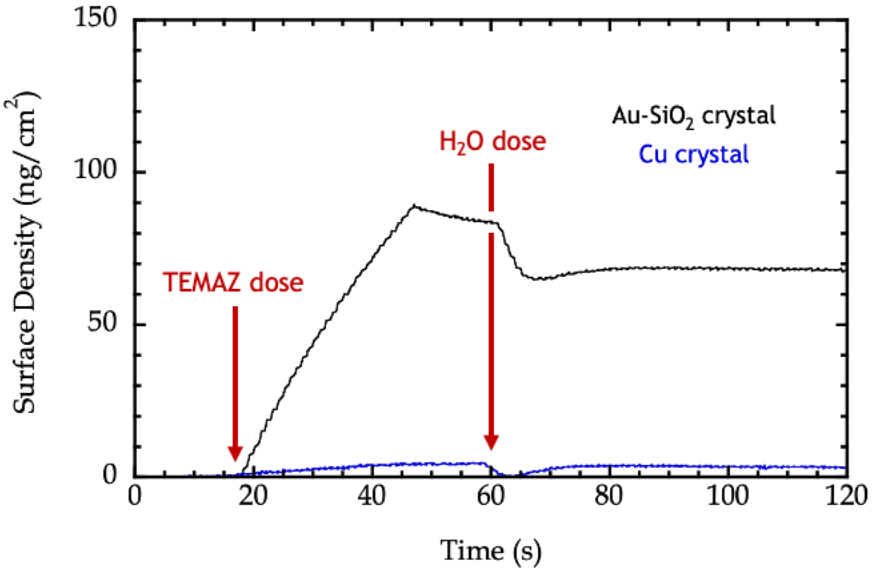

Figure 5-12 Zoomed-in QCM results at the 15th cycle of 30 cycles ZrO_2 ALD on Au-SiO_2 and Cu crystals

QCM results of ideally suppressed thin film growth on copper surface with ZrO_2 ALD are shown here. The experimental conditions are shown in Table 5-10. The process design was a sequence of pre-dose of water vapor, 20 cycles of ALD with 4-octyne during TEMAZ, 20 cycles pristine ALD, and then 20 cycles ALD with 4-octyne during TEMAZ. Suppressed growth should be expected during step 3 since a blocking layer should form on the copper surface. During step 4, the starting surface should be a clean copper surface once the 4-octyne flow stops (probably carbonaceous film in reality) and a growth is expected as a pristine ALD. For step 5, since the surface has altered to be zirconia (deposited film) and 4-octyne does not rehybridize well on oxides, it is very likely that there would be a mass uptake.

Results that has matched our theory are shown in Fig. 5-13. Film growth and cycle feature had been inhibited before 2460s (step 1-3). The constant GPC of pristine ALD was roughly 0.80 Å-cycle^{-1} from 2460s to 4860s (step 4), which was close to the reported values. Unknown mechanism for the mass uptake after 4860s (step5) but the hydroxyl group on the oxide surface was more reactive with the amine ligands from TEMAZ compared to 4-octyne, an alkyne if it existed. The mass uptake occurred after some extent of nucleation delay.

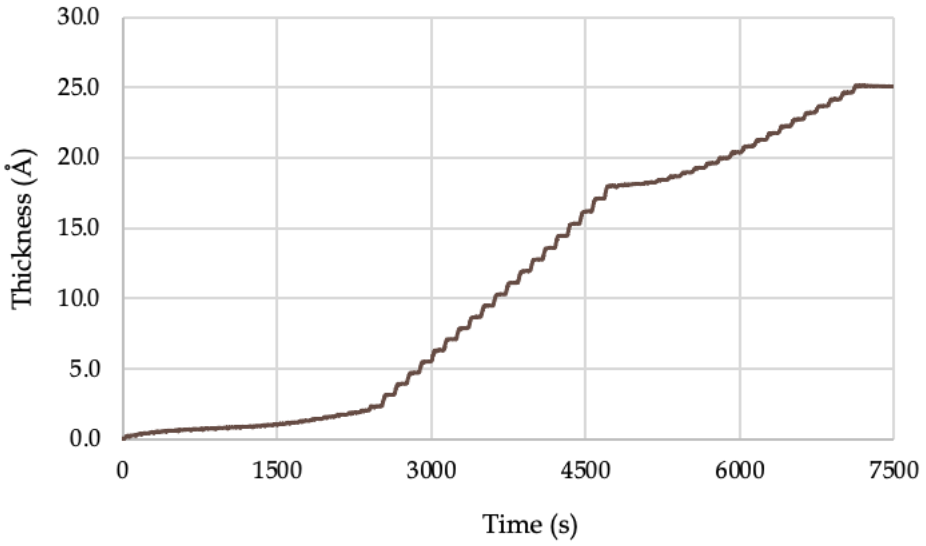

Figure 5-13 QCM results of ZrO_2 pristine ALD and ALD with 4-octyne during precursor on Cu crystal under the conditions shown in Table 5-10

With co-adsorbate / pristine / with co-adsorbate ZrO_2 ALD on Cu crystal		Panel	Carrier Flowrate (sccm)
		1-1	10
P (Torr)	1.5	2	21
T_s (°C)	120	3	21
Cycles	20, 20, 20	4	3
Exposure Sequence			
step	species	duration (s)	state
1	H_2O	10	co-reactant predose
2		50	purge
3-1	4-octyne	15	co-adsorbate
3-2	TEMAZ | 4-octyne	30	precursor & co-adsorbate
3-3	4-octyne	5	co-adsorbate
3-4		10	purge
3-5	H_2O	3	co-reactant
3-6		57	purge
4-1	TEMAZ	30	precursor
4-2		15	purge
4-3	H_2O	3	co-reactant
4-4		72	purge
5-1	4-octyne	15	co-adsorbate
5-2	TEMAZ | 4-octyne	30	precursor & co-adsorbate
5-3	4-octyne	5	co-adsorbate
5-4		10	purge
5-5	H_2O	3	co-reactant
5-6		57	purge

Table 5-10 Experimental conditions for ZrO_2 pristine ALD and ALD with 4-octyne during precursor with QCM system

Same experiment was conducted with step 1-4 in Table 5-10 and the results are shown in Fig. 5-14, which were reproducible. The GPC for step 3 (ALD with co-adsorbate, from 0s to 2460s) was 0.16 Å-cycle^{-1} while that for step 4 (pristine ALD, from 2460s to 4860s) was 0.79 Å-cycle^{-1}. As shown in Fig. 5-15 and Table. 5-11, the XPS results for the coupons under this experiment indicted that there was still deposition on both copper and chemox. However, the deposition thickness or GPC on both substrates were much lower and the thicknesses on Cu and

chemox substrates were comparable. Thickness on chemox should not be affected by 4-octyne and should be showing the same as that from 40 cycles of pristine ALD (~ 32Å), while the thickness on copper should be around 16Å (20cycles of pristine ALD). Another possibility was that there might be a significant surface contamination (i.e. air exposure) when transferring the samples. Thus for XPS analysis, it led to an attenuation of the substrate signals (a contamination layer on top) while electrons from Hf, the thin film signals, did not affect much within the analyzed range. The thickness from the substrate model would then be underestimated. Further studies are still required.

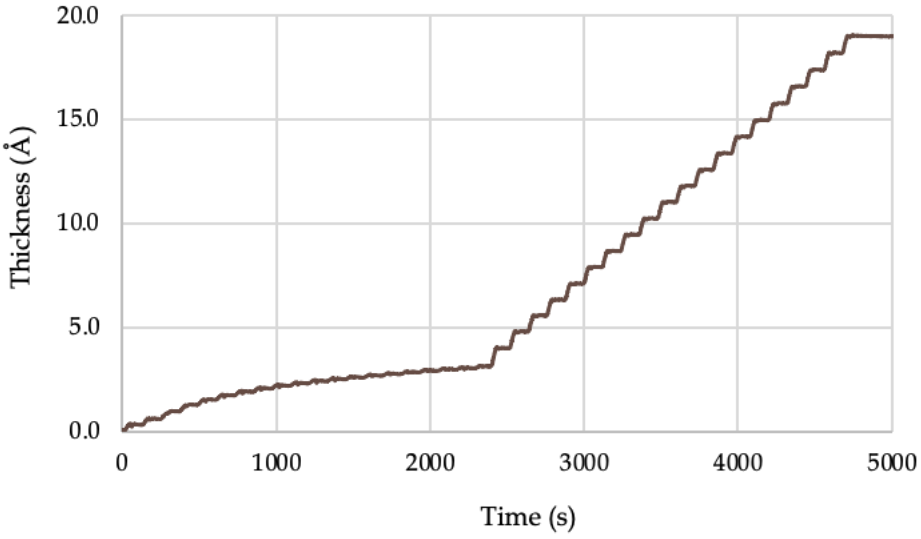

Figure 5-14 QCM results of ZrO_2 pristine ALD and ALD with 4-octyne during precursor on Cu crystal under the conditions from step 1 to 4 in Table 5-10

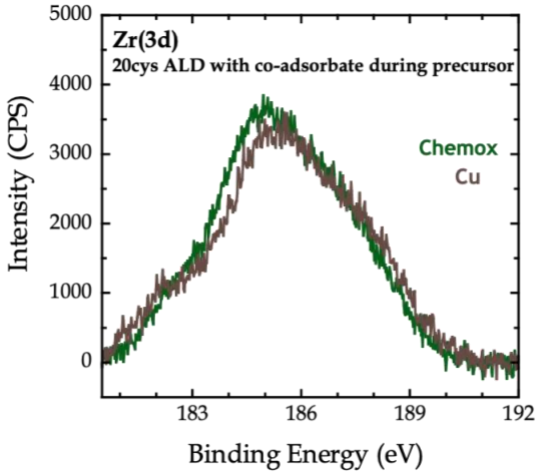

Figure 5-15 Zr(3d) XP spectra for ZrO_2 pristine ALD and ALD with 4-octyne during precursor on Cu and chemox substrates under the conditions shown in Table 5-10

	Sample	Intensity (raw area) [CPS-eV]					Sum [CPS-eV]	Peak BE [eV]	Peak KE [eV]	mfp[Å] in ZrO_2 with Mg(1249.1 eV)	ZrO_2 thickness [Å]	GPC [Å/cycle]
ALD with co-adsorbate	Cu	Cu metal	oxidized Cu (1)	oxidized Cu (2)				Cu(2p3/2)			10.17	0.51
		27070.4	472.013	3618.18			31160.59	932.75	316.35	8.36		
	Chemox	Si2p3/2	SiO2	Si2O3	SiO	Si2O		Si(2p3/2)			5.85	0.29
		5634.8	1562.37	81.0332	148.639	185.496	7612.34	97.96	1151.14	20.76		
180°C annealed Cu	Cu	Cu metal	oxidized Cu (1)	oxidized Cu (2)				Cu(2p) unattenuated base (substrate)				
		130574	6595.95	10190.8			147360.75					
180°C annealed Chemox	Chemox	Si2p3/2	SiO2	Si2O3	SiO	Si2O		Si(2p) unattenuated base (substrate)				
		9392.15	1518.37	0.001	0.001	0.001	10910.52					

Table 5-11 Thickness calculation for ZrO_2 pristine ALD and ALD with 4-octyne during precursor on Cu and chemox substrates under the conditions shown in Table 5-10

The experimental conditions for two HfO_2 ALD with micro-reactor system are shown in Table 5-12. One was conducted with H_2O as co-reactant at 180°C while the other one was with O_2 at 120°C. The XPS results are shown as (a) and (b) respectively in Fig. 5-16. Under the former conditions, the XP spectra for Cu(2p) and Si(2p) were showing fully attenuated, which indicated that both of these were semi-infinite films. First, it was explainable that the deposition was less under the latter conditions, since it should be less reactive at lower substrate

temperature and O_2 is a weaker oxidant than H_2O. Secondly, in either case, the deposition was not suppressed due to the introduction of 4-octyne on Cu surfaces; thus, more studies and adjustments on the experimental conditions are required.

HfO_2 ALD with co-adsorbate on Cu and native oxide coupons		**Panel**	**Carrier Flowrate (sccm)**
		curtain	49
P (Torr)	9	A	7
T_s (°C)	180 / 120	B	3.5
Cycles	5	C	7
Exposure Sequence			
step	**species**	**duration (s)**	**state**
1	4-octyne	60	co-adsorbate
2	TEMAHf | 4-octyne	120	precursor & co-adsorbate
3	4-octyne	30	co-adsorbate
4		20	purge
5	H_2O / O_2	10	co-reactant
6		180	purge

Table 5-12 Experimental conditions for HfO_2 ALD with 4-octyne during precursor with micro-reactor system (H_2O as co-reactant, at 180°C / O_2 as co-reactant, at 120°C)

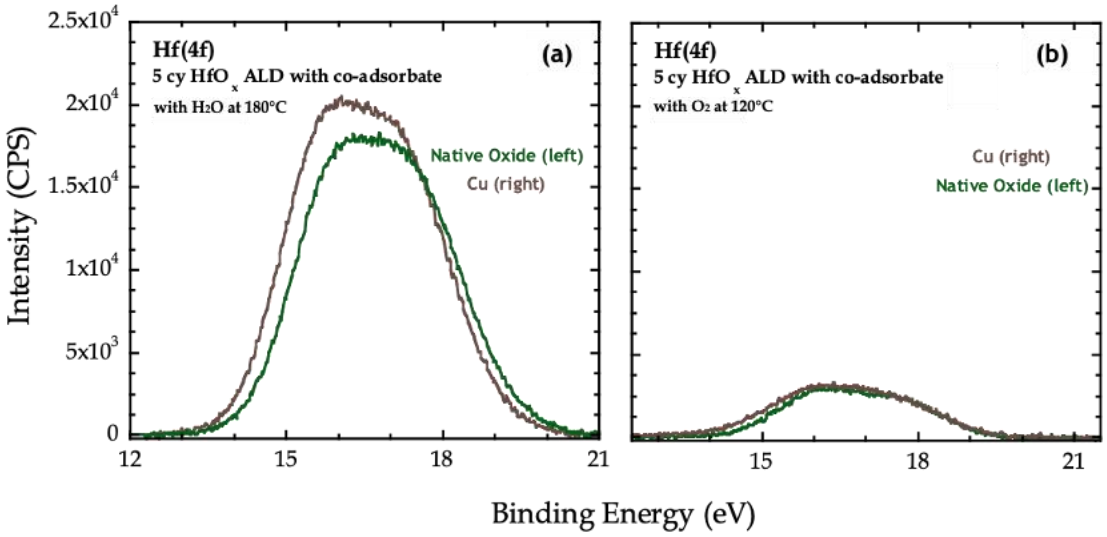

Figure 5-16 Hf(4f) XP spectra for HfO_2 ALD with 4-octyne during precursor on Cu and silica substrates under the conditions shown in Table 5-12 with (a) H_2O and at 180°C (b) O_2 and at 120°C

5.5.2 CVD with co-adsorbate

The experimental conditions for CVD with micro-reactor system are shown in Table 5-13. One for ZrO_2 CVD was conducted for 2s at step 3 while the other one for HfO_2 CVD was conducted for 5s. Another pristine HfO_2 CVD was conducted from step 2 to 4 without 4-octyne introduced and 5s at step 3. As shown in Fig. 5-17, the blocking effect had successfully been observed on cobalt surface under the presence of silica, although the deposition was minute. As shown in Fig. 5-18, the deposition on copper was slightly suppressed after 4-octyne was introduced. Though it was not fully suppressed and it might be overkilled due to the nucleation of the oxidants, these results could still support our theory and pave our way to the real selectivity.

CVD with co-adsorbate on Co, Cu and native oxide coupons		Panel	Carrier Flowrate (sccm)
		curtain	6
P (Torr)	1.5	A	3
T_s (°C)	120	B	3
		C	3
Exposure Sequence			
step	species	duration (s)	state
1	4-octyne	30	co-adsorbate
2	TEMAZ | 4-octyne	120	precursor & co-adsorbate
3	TEMAZ | 4-octyne | O_2	2 / 5	precursor, co-adsorbate and co-reactant
4	TEMAZ | 4-octyne	25	precursor & co-adsorbate
5	4-octyne	30	co-adsorbate

Table 5-13 Experimental conditions for ZrO_2 CVD with 4-octyne with micro-reactor system

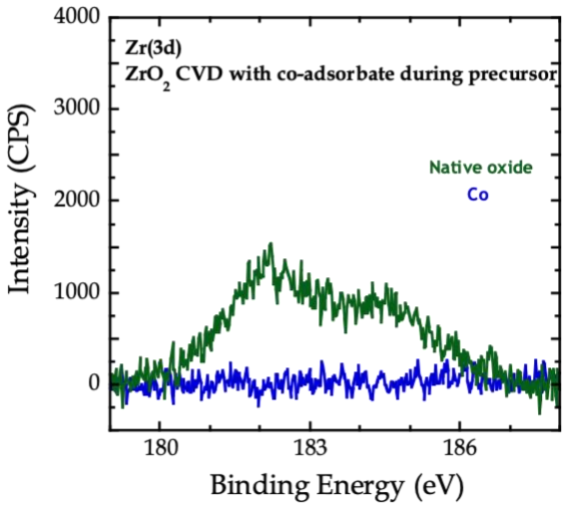

Figure 5-17 Zr(3d) XP spectra for ZrO_2 CVD with 4-octyne on silica and Co substrates under the conditions shown in Table 5-13 with 2s at step 3

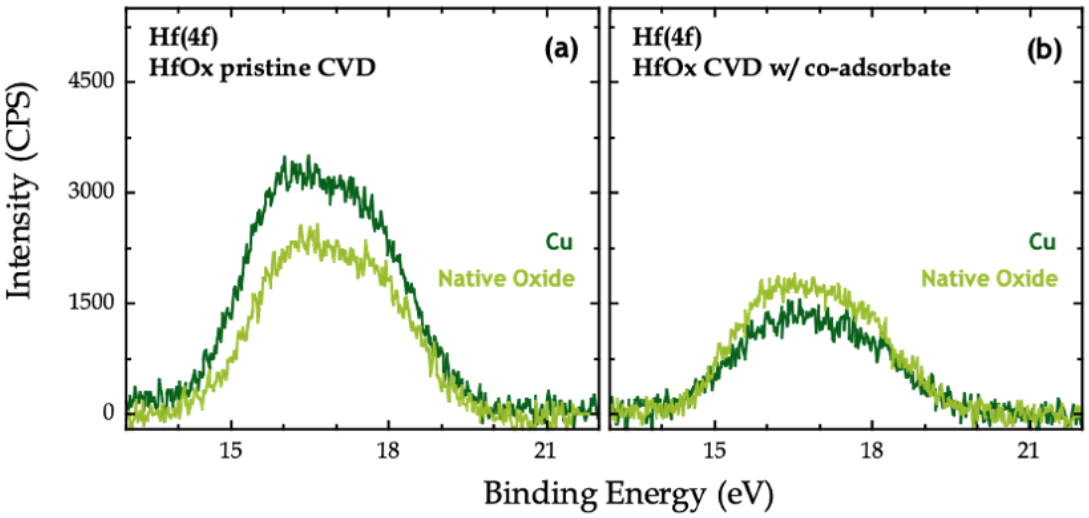

Figure 5-18 Hf(4f) XP spectra for HfO_2 (a) pristine HfO_2 CVD and (b) HfO_2 CVD with 4-octyne on Cu and silica substrates under the conditions shown in Table 5-13 with 5s for step 3

6. Conclusion

We have focused our work on the competitive adsorption of the co-adsorbate to achieve area-selective deposition. As the essential part in transistor fabrication, the technique to selectively deposit high-κ material on the dielectric channel instead of the metal interconnect system is the objective of our work to be applied to in the bottom-up manufacturing process. The selective deposition of HfO_2 and ZrO_2 on silica with TEMAHf and TEMAZ respectively was mainly studied with the introduction of 4-octyne. With the initial DFT calculations, several results had shown the potential and viability of this technique in both QCM and micro-reactor systems, although it was not definitive yet. Hardware modifications had also been implemented throughout the study in order to obtain the reproducibility and benign systems. For future work, various fabrication process could benefit from the selective deposition, such as an adhesion layer (TaN/Ta) on silica or a selective capping. Selective deposition for various combination of the precursors and purposes (such as MoD) could be utilized in the foundry industry; thus, it is a promising field of study.

7. Reference

[1] Łukasiak, L. & Jakubowski, A. History of Semiconductors.

[2] Parsons, G. N. & Clark, R. D. Area-Selective Deposition: Fundamentals, Applications, and Future Outlook. Chemistry of Materials 32, 4920–4953 (2020).

[3] Zaera, F. The surface chemistry of thin film atomic layer deposition (ALD) processes for electronic device manufacturing. Journal of Materials Chemistry 18, 3521–3526 (2008).

[4] Hausmann, D. M., Kim, E., Becker, J. & Gordon, R. G. Atomic Layer Deposition of Hafnium and Zirconium Oxides Using Metal Amide Precursors. (2002) doi:10.1021/cm020357x.

[5] Mackus, A. J. M., Merkx, M. J. M. & Kessels, W. M. M. From the Bottom-Up: Toward Area-Selective Atomic Layer Deposition with High Selectivity †. (2018) doi:10.1021/acs.chemmater.8b03454.

[6] Longo, R. C. et al. Selectivity of metal oxide atomic layer deposition on hydrogen terminated and oxidized Si(001)-(2×1) surface Atomic layer deposition of photoactive CoO/SrTiO3 and CoO/TiO2 on Si(001) for visible light driven photoelectrochemical water oxidation. Citation: Journal of Vacuum Science & Technology B 32, 84901 (2014).

[7] Mcdonnell, S. et al. Controlling the Atomic Layer Deposition of Titanium Dioxide on Silicon: Dependence on Surface Termination. (2013) doi:10.1021/jp4060022.

[8] MacKus, A. J. M., Leick, N., Baker, L. & Kessels, W. M. M. Catalytic combustion and dehydrogenation reactions during atomic layer deposition of platinum. Chemistry of Materials 24, 1752–1761 (2012).

[9] Pinna, N., Knez, M. & WILEY-VCH Verlag GmbH gc Co KGaA, W. Atomic Layer Deposition of Nanostructured Materials.

[10] Chopra, S. N., Zhang, Z., Kaihlanen, C. & Ekerdt, J. G. Selective Growth of Titanium Nitride on HfO 2 across Nanolines and Nanopillars. (2016) doi:10.1021/acs.chemmater.6b01036.

[11] Hughes, K. J. & Engstrom, J. R. Interfacial organic layers: Tailored surface chemistry for nucleation and growth. Journal of Vacuum Science & Technology A: Vacuum, Surfaces, and Films 28, 1033–1059 (2010).

[12] Färm, E., Kemell, M., Santala, E., Ritala, M. & Leskelä, M. Selective-Area Atomic Layer Deposition Using Poly(vinyl pyrrolidone) as a Passivation Layer. Journal of The Electrochemical Society 157, K10 (2010).

[13] Wilson, C. A., Grubbs, R. K. & George, S. M. Nucleation and growth during Al 2O 3 atomic layer deposition on polymers. Chemistry of Materials 17, 5625–5634 (2005).

[14] Hughes, K. J. & Engstrom, J. R. Nucleation delay in atomic layer deposition on a thin organic layer and the role of reaction thermochemistry. Journal of Vacuum Science & Technology A: Vacuum, Surfaces, and Films 30, 01A102 (2012).

[15] Zyulkov, I., Krishtab, M., de Gendt, S. & Armini, S. Selective Ru ALD as a Catalyst for Sub-Seven-Nanometer Bottom-Up Metal Interconnects. ACS Applied Materials and Interfaces 9, 31031–31041 (2017).

[16] Vaari, J., Lahtinen, J. & Hautojärvi, P. The adsorption and decomposition of acetylene on clean and K-covered Co(0001). Catalysis Letters 44, 43–49 (1997).

[17] Choi, J. H., Mao, Y. & Chang, J. P. Development of hafnium based high-k materials - A review. Materials Science and Engineering R: Reports vol. 72 97–136 (2011).

[18] Choudhury, D. et al. Atomic layer deposition of HfO 2 films using carbon-free tetrakis(tetrahydroborato)hafnium and water . Journal of Vacuum Science & Technology A 38, 042407 (2020).

[19] Johnson, R. W., Hultqvist, A. & Bent, S. F. A brief review of atomic layer deposition: from fundamentals to applications. Materials 17, (2014).

[20] Choi, J. H., Mao, Y. & Chang, J. P. Development of hafnium based high-k materials - A review. Materials Science and Engineering R: Reports vol. 72 97–136 (2011).

[21] Chen, T. et al. Novel zirconium precursors for atomic layer deposition of ZrO2 films. ECS Transactions 16, 87–101 (2008).

[22] Wallace, R. M., McIntyre, P. C., Kim, J. & Nishi, Y. Atomic layer deposition of dielectrics on ge and III-V materials for ultrahigh performance transistors. MRS Bulletin 34, 493–503 (2009).

[23] Suh, T. et al. Competitive Adsorption as a Route to Area-Selective Deposition. ACS Applied Materials and Interfaces 12, 9989–9999 (2020).

[24] Betteridge, W. The properties of metallic cobalt. Progress in Materials Science vol. 24 51–142 (1980).

[25] Lim, H. J., Saha, T., Tey, B. T., Tan, W. S. & Ooi, C. W. Quartz crystal microbalance-based biosensors as rapid diagnostic devices for infectious diseases. Biosensors and Bioelectronics vol. 168 112513 (2020).

[26] Cao-Paz, A., Rodriguez-Pardo, L. & Farina, J. Application of the QCM in lead acid batteries electrolyte measurements. in Procedia Engineering vol. 5 1260–1263 (Elsevier Ltd, 2010).

[27] Rahtu, A. & Ritala, M. Compensation of temperature effects in quartz crystal microbalance measurements. Applied Physics Letters 80, 521–523 (2002).

[28] Jurca, T. et al. Low-Temperature Atomic Layer Deposition of MoS2 Films. Angewandte Chemie - International Edition 56, 4991–4995 (2017).

[29] Holmqvist, A., Törndahl, T., Magnusson, F., Zimmermann, U. & Stenström, S. Dynamic parameter estimation of atomic layer deposition kinetics applied to in situ quartz crystal microbalance diagnostics. Chemical Engineering Science 111, 15–33 (2014).

[30] Avila, J. R. et al. Atomic layer deposition of Cu(i) oxide films using Cu(II) bis(dimethylamino-2-propoxide) and water. Dalton Transactions 46, 5790–5795 (2017).

[31] Sauerbrey, G. Verwendung von Schwingquarzen zur Wägung dünner Schichten und zur Mikrowägung. Zeitschrift für Physik 155, 206–222 (1959).

[32] Behrndt, K. H. Long-Term Operation of Crystal Oscillators in Thin-Film Deposition. Journal of Vacuum Science and Technology 8, 622–626 (1971).

[33] Lu, C. S. & Lewis, O. Investigation of film-thickness determination by oscillating quartz resonators with large mass load. Journal of Applied Physics 43, 4385–4390 (1972).

[34] Rocklein, M. N. & George, S. M. Temperature-induced apparent mass changes observed during quartz crystal microbalance measurements of atomic layer deposition. Analytical Chemistry 75, 4975–4982 (2003).

[35] R. Byron Bird, Warren E. Stewart, E. N. L. Transport Phenomena, Revised 2nd Edition. (John Wiley & Sons, Inc., 2006).

[36] Chen, J.-R., Zhang, W., Nahm, R. K., DiFeo, M. A. & Engstrom, J. R. Design and characterization of a microreactor for spatially confined atomic layer deposition and in situ UHV surface analysis . Journal of Vacuum Science & Technology A: Vacuum, Surfaces, and Films 35, 061604 (2017).

[37] Stevie, F. A. & Donley, C. L. Introduction to x-ray photoelectron spectroscopy. Journal of Vacuum Science & Technology A 38, 063204 (2020).

[38] Moulder, J. F., Stickle, W. F., Sobol, P. E. ', Bomben, K. D. & Chastain, J. Handbook of X-ray Photoelectron Spectroscopy AReference Book of Standard Spectra for Identification and Interpretation of XPS Data.

[39] Shirley, D. A. High-resolution x-ray photoemission spectrum of the valence bands of gold. Physical Review B 5, 4709–4714 (1972).

[40] Engelhard, M. H., Baer, D. R., Herrera-Gomez, A. & Sherwood, P. M. A. Introductory guide to backgrounds in XPS spectra and their impact on determining peak intensities. Journal of Vacuum Science & Technology A 38, 063203 (2020).

[41] Proctor, A. & Sherwood, P. M. A. Data Analysis Techniques in X-ray Photoelectron Spectroscopy. Analytical Chemistry 54, 13–19 (1982).

[42] Suh, T., Yang, Y., Sohn, H. W., Distasio, R. A. & Engstrom, J. R. Area-selective atomic layer deposition enabled by competitive adsorption. J. Vac. Sci. Technol. A 38, 62411 (2020).

[43] Hughes, K. J. The Initial Stages Of Atomic Layer Deposition On Substrates Modified By Organic Thin Films. Phys. Rev. E (2011).

[44] Brinker, C. J. & Scherer, G. W. Surface Chemistry and Chemical Modification. in Sol-Gel Science 616–672 (1990). doi:10.1016/b978-0-08-057103-4.50015-5.

[45] Zhuravlev, L. T. The surface chemistry of amorphous silica. Zhuravlev model. Colloids and Surfaces A: Physicochemical and Engineering Aspects 173, 1–38 (2000).

[46] Petitto, S. C. & Langell, M. A. Surface composition and structure of Co3O4(110) and the effect of impurity segregation. Journal of Vacuum Science & Technology A: Vacuum, Surfaces, and Films 22, 1690–1696 (2004).

[47] Chen, J. et al. Methanol decomposition on Co(0001): Influence of the cobalt oxidation state on reactivity. Journal of Physical Chemistry C 123, 9139–9145 (2019).

[48] Kizilkaya, A. C., Niemantsverdriet, J. W. & Weststrate, C. J. Oxygen Adsorption and Water Formation on Co(0001). Journal of Physical Chemistry C 120, 4833–4842 (2016).

[49] Keuter, T. et al. Atomic-layer-controlled deposition of TEMAZ/O2-ZrO2 oxidation resistance inner surface coatings for solid oxide fuel cells. Surface and Coatings Technology 288, 211–220 (2016).

[50] Provine, J. et al. Atomic layer deposition by reaction of molecular oxygen with tetrakisdimethylamido-metal precursors. Journal of Vacuum Science & Technology A: Vacuum, Surfaces, and Films 34, 01A138 (2016).

[51] Dueñas, S. et al. Comparative study on electrical properties of atomic layer deposited high-permittivity materials on silicon substrates. Thin Solid Films 474, 222–229 (2005).

[52] Kukli, K., Ritala, M., Lu, J., Hårsta, A. & Leskelä, M. Properties of HfO2 Thin Films Grown by ALD from Hafnium tetrakis(ethylmethylamide) and Water. Journal of The Electrochemical Society 151, F189 (2004).